

Discovering Mechanistic Models of Neural Activity: System Identification in an *in Silico* Zebrafish

Jan-Matthis Lueckmann¹, Viren Jain¹ and Michał Januszewski¹

¹Google Research

Constructing mechanistic models of neural circuits is a fundamental goal of neuroscience, yet verifying such models is limited by the lack of ground truth. To rigorously test model discovery, we establish an *in silico* testbed using neuromechanical simulations of a larval zebrafish as a transparent ground truth. We find that LLM-based tree search autonomously discovers predictive models that significantly outperform established forecasting baselines. Conditioning on sensory drive is necessary but not sufficient for faithful system identification, as models exploit statistical shortcuts. Structural priors prove essential for enabling robust out-of-distribution generalization and recovery of interpretable mechanistic models. Our insights provide guidance for modeling real-world neural recordings and offer a broader template for AI-driven scientific discovery.

1. Introduction

A fundamental goal in neuroscience is to understand how neural circuits process information and generate behavior. The ability to predict neural activity is a key test towards such understanding. Data-driven benchmarks can accelerate progress by providing standardized datasets and evaluation metrics (Schrimpf et al., 2020; Pei et al., 2021; Turishcheva et al., 2023; Lueckmann et al., 2025).

However, benchmarks relying on real experimental data face inherent limitations and verification challenges. For instance, limitations include the high cost and technical difficulty of acquiring large-scale, high-resolution neural recordings, the presence of noise and unobserved variables, and restrictions in systematically manipulating neural circuits or environments. Real-world experiments that involve imaging of neural activity are severely restricted in duration and throughput (e.g., due to phototoxicity, molecular reporters, and imaging limitations), and subject to artifacts and preprocessing challenges (e.g., motion, striping, imperfect alignment and segmentation). More fundamentally, much about the underlying biological systems used in such benchmarks is as yet unknown (e.g., the detailed connectivity of underlying circuits, synaptic release probabilities, neuromodulatory interactions). Therefore, since the ground-truth data-generating process is unknown, models are ranked relative to each other rather than compared against an absolute reference. It is thus unclear how far models are from the true mechanisms of computation, or whether they have identified statistical shortcuts. This creates a verification gap: without a known ground truth, it is hard to rigorously evaluate models and model discovery strategies.

Neuromechanical simulations provide a powerful avenue to complement real-data benchmarks: Embodied simulations can generate vast amounts of perfectly annotated data where the underlying “ground truth” of the neural system is known and controllable. They allow for systematic manipulation of physiological and circuit features that are difficult or impossible to achieve in biological experiments—offering full observability and control over factors such as dataset dimensionality, length, and noise levels, along with the ability to perturb any part of their neural circuitry. *simZFish* (Liu et al., 2025), an open-source neuromechanical simulation of the larval zebrafish, is one such platform that realistically models the fish’s body, its physical interactions with the environment, visual inputs, and experimentally

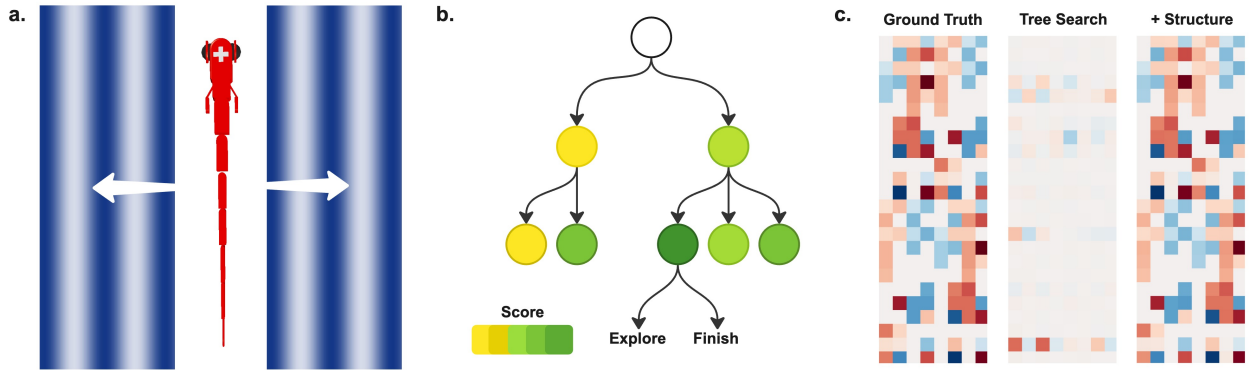


Figure 1 | Verifiable discovery of neural mechanisms in an *in silico* testbed. **a.** The simulation environment consists of a neuromechanical model subject to fluid dynamics, responding to visual stimuli driven by a neural circuit in a closed-loop setting. **b.** We use LLM-guided tree search to autonomously explore the space of dynamical models, evolving Python code to minimize predictive error on neural activity. **c.** Despite high predictive in-distribution performance, unconstrained black-box tree search models fail to identify the system’s mechanisms, as revealed by effective connectivity matrices (excerpt shown; blue and red indicate inhibitory and excitatory interactions, respectively; color intensity represents magnitude). In contrast, a structure-constrained grey-box tree search model successfully identifies the correct signs and magnitudes closely matching the ground truth, from a structural prior that provides information about the existence and absence of connections.

constrained neural architectures for visuomotor behaviors.

In this work, we use simZFish to generate high-fidelity *in silico* datasets that serve as a testbed for system identification (Ljung, 2010). By simulating the virtual fish’s response to a range of visual stimuli, we create a ground-truth dataset where every internal state, sensory input, and underlying circuit connectivity is perfectly observable. This allows us to study a critical question: What are the data and modeling prerequisites to recover the mechanisms of a complex neural circuit?

While standard forecasting architectures can provide initial baselines, they are rarely optimized for the specific temporal and structural constraints of neural dynamics. A primary bottleneck in modeling neural activity is often the modeler’s own inductive bias and the significant time required to manually explore the architectural landscape. We address this by framing model design as an optimization problem. Specifically, we utilize an automated tree-search approach (Aygün et al., 2025) to traverse a vast space of code-based model definitions, leveraging Large Language Models (LLMs) to effectively “evolve” solutions. We compare two distinct discovery regimes: an unconstrained search for high-accuracy black-box predictors, and a structure-constrained search that uses structural priors (derived from the “wiring diagram”), and we evaluate the discovered models with respect to their ability to generalize to unseen stimuli, their interpretability, and mechanistic recovery (Figure 1).

In summary, our contributions are as follows:

1. **An *in silico* testbed for verifiable neural system identification.** Unlike real-data benchmarks where ground truth is unknown, our testbed provides a transparent reference, allowing us to evaluate whether models recover the true mechanisms of a neural circuit.
2. **Sensory drive is a prerequisite for identifiability.** We demonstrate that in sensory-driven neural circuits, the true transition function is practically non-identifiable using standard autoregressive history alone.

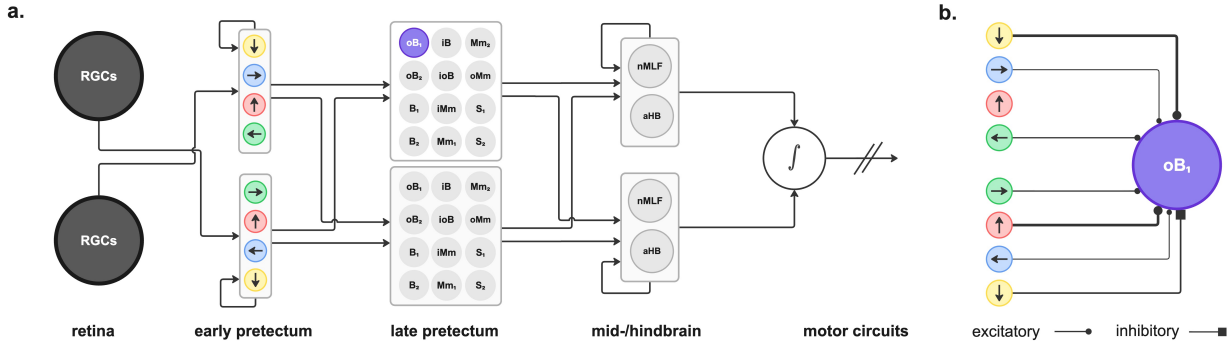


Figure 2 | Neural circuit model. **a.** The neural circuit model defines the information flow, processing retinal input through the early and late pretectum (ePT, IPT) to drive downstream command nuclei (nMLF, aHB) and motor circuits. **b.** Connectivity diagram of an example late pretectal neuron (oB_1), illustrating the specific excitatory and inhibitory wiring with ePT neurons resulting in its direction-selectivity.

3. **In-distribution accuracy is a poor proxy for system identification.** We show that LLM-guided tree search discovers models that achieve state-of-the-art test set accuracy but fail on out-of-distribution (OOD) stimuli. These models prioritize statistical shortcuts over faithful recovery of mechanisms, challenging the practice of ranking neural models by test set error.
4. **Structural priors enable mechanistic recovery.** We demonstrate that providing structural priors is sufficient to regularize the discovery process. This eliminates statistical shortcuts, enables robust OOD generalization, interpretability, and faithful recovery of static and dynamic mechanisms—as verified by effective connectivity and impulse response analyses, respectively.
5. **Recommendations for real-world system identification:** Based on our *in silico* results, we propose concrete guidelines for modeling real neural recordings. We recommend shifting from pure autoregression to connectome-constrained conditional forecasting tasks with OOD evaluations, to bridge the gap between predictive AI and mechanistic neuroscience.

We position our work relative to recent advances in automated model discovery, neural system identification, and connectome-constrained modeling in [Appendix A](#).

2. Methods

2.1. Neuromechanical Simulations

We generate synthetic neural activity datasets with simZFish, a detailed neuromechanical simulator of larval zebrafish [Liu et al. \(2025\)](#). It integrates realistic body mechanics, environmental interactions, and neural circuits to reproduce sensorimotor behaviors like the optomotor response (OMR). The OMR is an innate reflex causing fish to orient in the direction of whole-field visual motion to stabilize position, and it is probed in openly available whole-brain activity recordings (e.g., [Chen et al., 2018](#); [Lueckmann et al., 2025](#)). We provide a summary of the simulations, and refer to [Liu et al. \(2025\)](#) and [Appendix B](#) for full details.

2.1.1. Simulation Environment

Simulations are implemented in Webots ([Michel, 2004](#)), an open-source robotics simulator. An illustration of the simulation environment is in [Figure 1a](#).

Body Model. The body approximates a 4 mm larval zebrafish with density slightly less than water. It comprises seven cuboid segments—a head with cameras and pectoral fins, followed by six body segments, and a tail fin—connected by servomotor-actuated hinge joints.

Sensory Environment. Visual stimuli (drifting sinusoidal gratings) are presented in a simulated petri dish, locked to the body orientation, mimicking closed-loop setups.

Fluid Dynamics. To simulate realistic locomotion, the body is subject to buoyancy, viscous resistance, and inertial drag, with parameters tuned to match kinetic recordings.

Our simulations employ a 0.05 ms integration time step using Webots' default first-order semi-implicit integrator for the body kinematics.

2.1.2. Neural Circuit Model

The neural circuit model is based on anatomical, functional, and computational findings from real zebrafish visuomotor pathways. We ported the C-based implementation by [Liu et al. \(2025\)](#) to JAX ([Bradbury et al., 2018](#)), for differentiability and ease of experimentation. An overview of the network model is in [Figure 2](#).

The circuit is formulated as a dynamical system where the activity of a neural population is determined by a non-linear transition operator. We define a generalized sigmoidal response function, Φ , parameterized by synaptic weights \mathbf{W} , bias thresholds \mathbf{b} , and response gains ω :

$$\Phi(\mathbf{x}; \mathbf{W}, \mathbf{b}, \omega) = \sigma(\omega \odot (\mathbf{W}\mathbf{x} - \mathbf{b})), \quad (1)$$

where \mathbf{x} is the input vector, $\sigma(\cdot)$ is the element-wise sigmoid function, and \odot denotes the Hadamard product.

Retina. Visual input is captured by two laterally positioned simulated cameras, acting as photoreceptors driving a layer of simulated Bipolar Cells (BCs) detecting transient luminance changes. BCs project to four types of Direction-Selective Retinal Ganglion Cells (DSGCs), tuned to the four cardinal directions, producing an output vector $\mathbf{u}_t^{\text{ret}}$ representing the instantaneous motion across the visual field.

Early Pretectum. The retinal output projects contralaterally to the Early Pretectum (ePT). Unlike the retina, pretectal responses exhibit significant temporal persistence. The ePT state $\mathbf{h}_t^{\text{ept}}$ is defined as a first-order low-pass filter driven by sparse retinotopic projections:

$$\mathbf{h}_t^{\text{ept}} = (1 - \alpha_t)\mathbf{h}_{t-1}^{\text{ept}} + \alpha_t \Phi(\mathbf{u}_t^{\text{ret}}; \mathbf{W}_{\text{ret}}, \mathbf{b}_{\text{ept}}, \omega_{\text{ept}}), \quad (2)$$

where \mathbf{W}_{ret} is a fixed, sparse binary mask enforcing contralateral connectivity to the lower-temporal visual field. Crucially, the update rate α_t is state-dependent: its value depends on the current motor state (swim bout vs. rest) to dynamically filter out self-generated visual motion artifacts during rapid tail beats.

Late Pretectum. The ePT neurons drive the Late Pretectum (lPT), a layer responsible for synthesizing complex binocular motion primitives. This layer consists of 12 distinct functional types per hemisphere, whose names reflect three axes of variation: (1) direction (inward/outward/global); (2) ocularity (monocular/binocular); and (3) velocity preference (type 1/type 2; forward- vs. backward-preferring). For example, an oB₁ neuron responds to outward binocular motion and prefers forward velocity.

Mathematically, we model the lPT as an instantaneous layer combining linear connectivity with a non-linear binocular gating mechanism. We express this compactly by treating the gating signal as a

state-dependent threshold modulation:

$$\mathbf{h}_t^{\text{lpt}} = \Phi \left(\mathbf{h}_t^{\text{ept}}; \mathbf{W}_{\text{lpt}}, \mathbf{b}_{\text{lpt}} - \mathbf{M}_{\text{gate}} \odot \mathbf{g}(\mathbf{h}_t^{\text{ept}}), \boldsymbol{\omega}_{\text{lpt}} \right). \quad (3)$$

Here, \mathbf{W}_{lpt} encodes the subtype-specific excitatory/inhibitory wiring (e.g., [Figure 2b](#)). The term $\mathbf{g}(\cdot)$ represents a binocular co-activation signal (AND-gate) implemented via a minimum function that selects specific pairs of ipsilateral and contralateral inputs (see [Appendix B](#) for details). This modulation effectively acts as a dynamic bias, controlled by the sparse mask \mathbf{M}_{gate} (active only for two lPT neurons per hemisphere).

Command Neurons in Mid- and Hindbrain (CMD). The lPT layer projects to two downstream command centers: the Nucleus of the Medial Longitudinal Fasciculus (nMLF) controls swim vigor, and the Anterior Hindbrain (aHB), controlling turning bias. They are modeled as first-order low-pass filters with distinct timescales β and connectivity:

$$\mathbf{h}_t^{\text{cmd}} = (1 - \beta) \mathbf{h}_{t-1}^{\text{cmd}} + \beta \Phi(\mathbf{h}_t^{\text{lpt}}; \mathbf{W}_{\text{cmd}}, \mathbf{b}_{\text{cmd}}, \boldsymbol{\omega}_{\text{cmd}}). \quad (4)$$

While the nMLF integrates inputs to drive forward velocity, aHB integrates bilateral differences for the turning direction.

Motor Circuits. Locomotion in zebrafish is discrete (burst-and-glide). The “Bout Gate” is implemented as a stochastic Integrate-and-Fire mechanism. An evidence accumulator I_t integrates the total drive from the nMLF:

$$I_t = I_{t-1} + \gamma \sum_{i=1}^2 h_{t,i}^{\text{cmd}} + \epsilon_t, \quad \epsilon_t \sim \mathcal{N}(0, \sigma^2). \quad (5)$$

A swim bout is triggered if I_t exceeds a threshold θ , resetting the integrator. Upon initiation, the discrete action $a_t \in \{\text{Forward, Left, Right}\}$ is sampled from a categorical distribution determined by the command neuron states, with action probabilities \mathbf{p}_t :

$$\mathbf{p}_t = \frac{\mathbf{s}_t}{\|\mathbf{s}_t\|_1} \quad \text{with} \quad \mathbf{s}_t = \mathbf{W}_{\text{act}} \mathbf{h}_t^{\text{cmd}} + \mathbf{b}_{\text{act}}. \quad (6)$$

When the “Behavior Determinator” initiates a turn, it triggers greater activity in the ventral spinal neurons (vSPN) on one side, which in turn leads to increased ipsilateral motor neuron activation and the necessary body curvature for the turn. Finally, twelve spinal central pattern generators (CPGs), modeled as coupled oscillators, generate rhythmic tail undulations, and twelve motor neurons determine body curvature by integrating outputs from vSPNs and CPGs.

2.1.3. Simulated Behavior

The simulated fish executes discrete bouts consisting of rapid tail undulations followed by a passive glide phase, similar to real zebrafish. When exposed to drifting sinusoidal gratings, it recapitulates the behavioral distribution of swims and turns observed in real zebrafish.

2.1.4. Dataset Generation

We ran simZFish simulations under four binocular motion conditions designed to probe the visuomotor circuit: bilateral outward, bilateral inward, and two asymmetric configurations where eyes receive opposing inward/outward motion. At the same time, we recorded the activity, resulting in 400,000 samples at 1 ms resolution in total.

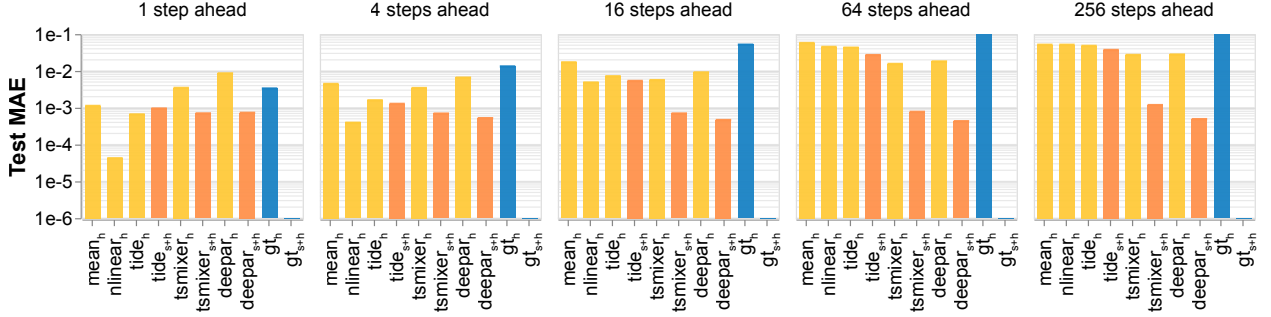


Figure 3 | **Sensory information is a prerequisite for system identification.** Performance (Test MAE, log scale) of baseline models and the gt circuit across prediction horizons. While models marked with $s+h$ are conditioned on exogenous sensory drive, models with h only use past history. gt_h yields higher error than the naive $mean_h$ baseline, suggesting that the true solution is non-identifiable without sensory drive based on standard error metrics.

2.2. System Identification

To provide a foundation for verifiable model discovery, we establish a task using the simZFish dataset.

2.2.1. Task Definition

We frame our task as a system identification problem (Ljung, 2010). We assume the neural activity evolves according to a ground-truth transition function f^* driven by past activity and sensory information:

$$\mathbf{a}_t = f^*(\mathbf{a}_{t-1}, \mathbf{x}_t), \quad (7)$$

where $\mathbf{a}_t \in \mathbb{R}^N$ is the activity of the $N = 36$ neural units (comprised of ePT, lPT, and nMLF/aHB populations) and $\mathbf{x}_t \in \mathbb{R}^D$ represents the exogenous covariates. The covariates include variables that drive the system but are not targets of prediction: specifically the instantaneous sensory drive $\Phi(\mathbf{u}_t^{\text{ret}})$ and the behavioral bout state. Because the internal bout trigger is stochastic (Equation 5), the future trajectory contains inherent (aleatoric) uncertainty. Conditioning on \mathbf{x} resolves this, transforming the task from a probabilistic into a deterministic problem.

We seek to discover a parameterized model f_θ that approximates the mechanisms of f^* . Since the ground-truth mechanisms are unknown in real-world settings, we do not optimize for mechanistic similarity directly. Instead, we employ multi-step forecasting as a proxy task. The identification task is to find the optimal pair (f, θ) that minimizes the divergence between the recursively simulated trajectory $\hat{\mathbf{a}}$ and the ground truth \mathbf{a} over a horizon $H = 256$:

$$\min_{\theta} \sum_{t=1}^H \|\hat{\mathbf{a}}_t - \mathbf{a}_t\| \quad \text{s.t.} \quad \hat{\mathbf{a}}_t = f_\theta(\hat{\mathbf{a}}_{t-1}, \mathbf{x}_t). \quad (8)$$

To test for both interpolation and robust extrapolation, we use three of the conditions described in Section 2.1.4 for the in-distribution regime (split chronologically into 70% training, 10% validation, and 20% test), while the fourth is reserved as an out-of-distribution (OOD) holdout to evaluate whether models generalize.

2.2.2. Evaluation

We evaluate candidate models on two axes: their ability to predict neural activity and their success in recovering ground-truth mechanisms.

Following ZAPBench (Lueckmann et al., 2025), we quantify trajectory prediction error using the Mean Absolute Error (MAE) averaged across all units and time steps. For a set of test windows \mathcal{W} , the error is defined as:

$$\text{MAE}_{\mathcal{W}} = \frac{1}{|\mathcal{W}|} \sum_{w \in \mathcal{W}} \frac{1}{N} \sum_{n=1}^N \frac{1}{H} \sum_{h=1}^H |\hat{a}_{h,n}^w - a_{h,n}^w|. \quad (9)$$

We report this metric on two data splits. The Test MAE measures performance on held-out trajectories from the same stimulus conditions used during training. The Holdout MAE measures performance on the OOD stimulus condition. We posit that a low Holdout MAE is a strong proxy for having learned the correct mechanisms.

Since we operate in an *in silico* setting with known, differentiable ground truth f^* , we can verify the mechanistic fidelity of a discovered model f_θ : We compute the effective connectivity matrix using Jacobian sensitivity analysis and impulse responses (IR) relative to f^* . This allows us to evaluate recovery of static and dynamic mechanisms, respectively. [Appendix C](#) provides details on these analyses including computation of the error metrics \mathcal{L}_{Jac} and \mathcal{L}_{IR} .

2.3. Baseline Models

To contextualize the performance of our discovered models, we compare against two distinct categories of baselines. First, to establish the predictive ceiling of the dataset, we employ state-of-the-art time-series forecasting architectures including nlinear (Zeng et al., 2023), tide (Das et al., 2023), and tsmixer (Chen et al., 2023), as well as a naive mean baseline. These models map a history window directly to the future horizon without explicitly modeling step-by-step transition dynamics. While they serve as rigorous controls for predictive accuracy, they do not yield an explicit transition function. Second, we evaluate deepar (Salinas et al., 2020), a probabilistic recurrent network. Like our discovered models, deepar recursively predicts the next step via a learned transition function. Details are in [Appendix D](#).

2.4. Tree Search

To navigate the combinatorial space of potential neural architectures, we employ an automated code generation approach driven by LLMs and Tree Search: We use the method proposed by Aygün et al. (2025), which combines a pre-trained LLM with a heuristic search algorithm (Predictor Upper Confidence Bound; Silver et al., 2016) to iteratively refine solutions. The search scores solution using validation set MAE on in-distribution conditions. We utilized Gemini 3 Flash (Google, 2025) as the backbone LLM. All details are in [Appendix E](#).

2.5. Data and Code

We will release datasets and code, including the JAX-translated neural circuit model, upon publication.

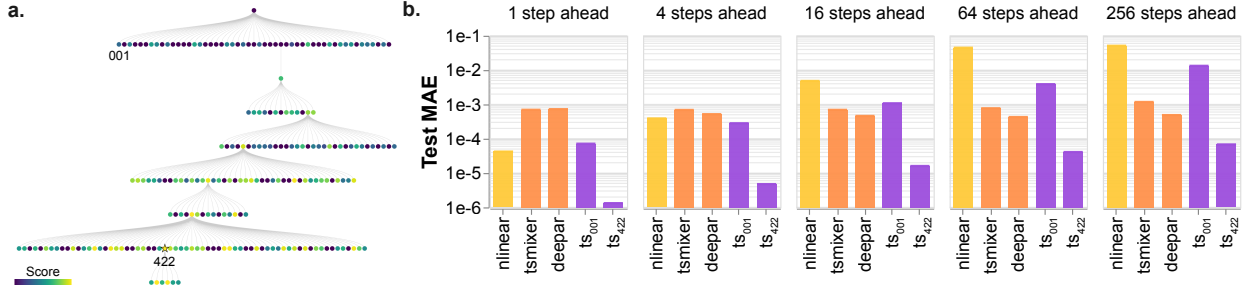


Figure 4 | Tree search discovers SOTA predictive models. **a.** Progression of LLM-guided tree search, highlighting first and highest-scoring solutions (ts_{001} , ts_{422}). For visual clarity, this tree is pruned to show only the ancestral path of ts_{422} ; the complete, unpruned search tree is in [Figure S1](#). **b.** Performance comparison of discovered models against human-curated baselines. The highest-scoring discovered tree-search architecture (ts_{422}) significantly outperforms baselines across all prediction horizons.

3. Results

3.1. Sensory Drive and Identifiability

A fundamental challenge in neural modeling is distinguishing intrinsic dynamics from responses to extrinsic drive ([Vahidi et al., 2024](#)). We used our *in silico* testbed to perform this decomposition explicitly—an intervention virtually impossible to replicate in real-world experiments. We evaluated a model reflecting the ground truth circuit in two regimes: conditioned on instantaneous sensory drive and the history of past activity (gt_{s+h}), and a control for which the sensory drive $\Phi(\mathbf{u}_t^{ret})$ is set to zero (gt_h).

Despite using the true transition function f^* , gt_h yields higher error than the naive $mean_h$ baseline ([Figure 3](#)). This apparent paradox highlights the dissipative nature of the system: without sensory drive, the underlying circuit dynamics decay to rest. In contrast, the $mean_h$ baseline minimizes error by predicting that neural activity persists unchanged—thereby reflecting the average activity maintained by the continuous sensory drive. This shows that in a purely autoregressive setting, the true mechanistic model is practically non-identifiable based on standard error metrics. Only when conditioning on sensory drive in addition to history is the system identification task well-posed: The error for gt_{s+h} drops to the numerical floor, representing the limits of floating-point precision.

However, access to sensory drive is necessary but not sufficient; the model architecture must also be capable of effectively utilizing it. While the multivariate $tsmixer_{s+h}$ and $depar_{s+h}$ baselines improve with the addition of sensory covariates, the univariate $tide_{s+h}$ model does not significantly improve over its history-only counterpart, $tide_h$. This disparity highlights a representational mismatch: the visual stimulus is a global signal that exerts differential effects across the population. Global univariate models like $tide$ —which apply a shared mapping across all units—lack the expressivity to capture how a single global input drives heterogeneous neural responses.

3.2. Model Discovery with Tree Search

The search space of predictive architectures is vast, encompassing a wide variety of structural biases, connectivity patterns, and temporal integration strategies. Traditionally, navigating this space relies on researcher intuition and manual trial-and-error. To evaluate whether automated discovery can identify accurate models of neural dynamics, we utilized an LLM-guided tree search.

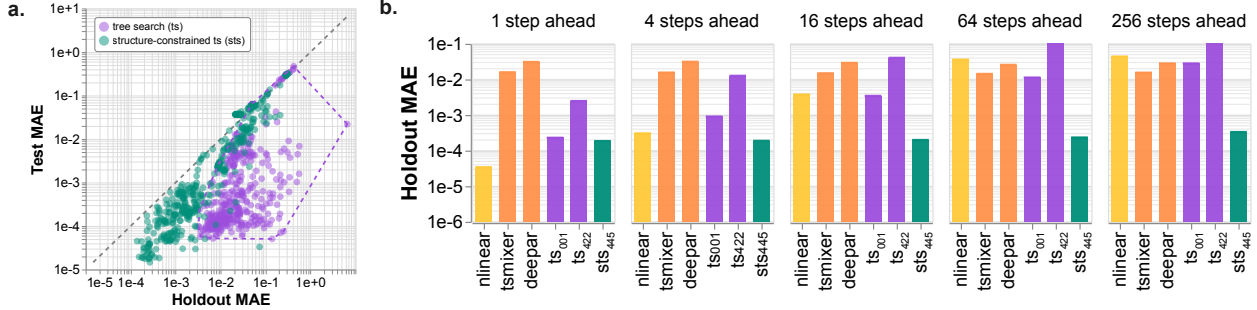


Figure 5 | Structural priors enable robust generalization. **a.** Generalization analysis comparing performance on in-distribution (Test MAE) versus out-of-distribution stimuli (Holdout MAE). Tree search models (ts, purple) exhibit a significant generalization gap; while they achieve high accuracy on the test set, they fail to generalize to novel stimuli, suggesting they memorize sensory-motor correlations. Structurally-constrained tree search solutions (sts, green) cluster closer along the diagonal, indicating robust transfer to unseen environments. Dotted purple line marks the convex hull for ts solutions. **b.** Holdout performance across prediction horizons. The highest-scoring constrained model (sts₄₄₅) significantly outperforms its unconstrained counterpart (ts₄₂₂) and baselines.

In our initial experiments, tree search tended to produce heterogeneous code across various frameworks, making systematic evaluation and integration difficult. We developed a standardized evaluation harness and prompt designed specifically to search within the class of autoregressive models implemented in flax (Heek et al., 2024). To ensure the discovery process remained computationally efficient, we implemented a heavily optimized, GPU-resident data loading pipeline. We found that training models on a truncated rollout of 32 timesteps was sufficient to identify architectures that performed well on the full 256-step prediction horizon, significantly reducing the training time required for each candidate solution during the search process.

Following these changes, the automated discovery process Figure 4a was highly successful, with many of the identified solutions achieving significantly lower Test MAE than the predictive baselines: Figure 4b highlights the performance of two discovered models, ts₀₀₁ (the first AI-generated solution) and ts₄₂₂, compared to nlinear, tsmixer, and deepar. Notably, ts₄₂₂ represents the highest-scoring outcome of our search, outperforming state-of-the-art baselines by almost an order of magnitude when averaging over all prediction horizons.

3.3. Generalization and Interpretability

Despite the high predictive accuracy of the tree-search models, they have limited scientific utility: they fail to generalize and it is unclear how to map them to the underlying circuit.

As shown in Figure 5a, unconstrained tree-search models (ts) with low Test MAE exhibit a significant generalization gap. Although they achieve near-perfect MAE on the test set for trained stimulus conditions, their performance degrades sharply when evaluated on held-out visual stimuli. This indicates that the search identifies solutions that exploit stimulus-specific correlations—essentially capturing statistical shortcuts—rather than recovering mechanisms that govern the zebrafish’s response.

Furthermore, these solutions offer limited interpretability for the computational neuroscientist. In Appendix F.3, we show the transition function for the highest-scoring model, ts₄₂₂. While the code is mathematically precise, it is mechanistically opaque. The transition function lacks a clear correspondence to the neural circuit and instead makes its predictions in a 256-dimensional latent

space. This lack of mechanistic transparency makes it difficult to map the model’s internal operations back to the physical circuit, rendering it of limited value for formulating testable biological hypotheses.

3.4. Incorporating Structural Priors

To bridge the gap between predictive accuracy and scientific utility, we modified the discovery process by incorporating structural priors. Instead of an unconstrained search over transition functions, we provided the tree search with prior information derived from the structural connectivity of the neural circuit (Appendix E.3): These hints reveal the system’s hierarchical organization, the sparse connectivity patterns (including recurrence) and the functional role of covariates. Crucially, the structural prior provided to the search contains no information about connectivity weights—only about the existence and absence of connections. The specific non-linear functions that govern the interactions must still be discovered.

The impact of the structural prior is clearly evident in the model’s ability to generalize. As shown in Figure 5a, structure-constrained models (green markers, sts) are closer to the diagonal region of the scatter plot. Unlike the unconstrained models, sts solutions maintain more consistent performance across both training and held-out stimulus conditions, suggesting that they overfit less to correlations present in train and test sets. The highest-scoring model (sts₄₄₅) is significantly more robust on the OOD condition, more than an order of magnitude for longer prediction horizons compared to baselines (Figure 5b).

In Appendix F.4, we show the transition function for sts₄₄₅: In contrast to the hard-to-interpret code of ts₄₂₂, it reflects the structural organization of the circuit and is composed of semantically meaningful motifs.

3.5. Mechanistic Recovery

We analyzed the effective connectivity of the highest-scoring discovered solution to evaluate mechanistic recovery (Appendix C.1). In the ground truth circuit (Figure 6a), the lPT population depends on structured inputs from the ePT population (middle-left block). The unconstrained ts₄₂₂ model (Figure 6b) fails to recover these upstream dependencies. Instead, it relies on spurious recurrence within the lPT population (central block)—effectively substituting internal memory for sensory processing.

In contrast, sts₄₄₅ recovers the correct effective connectivity. While the structural prior included a binary matrix for ePT → lPT connectivity and indicated absence of recurrent lPT connections, it contained no information about the strengths of the feedforward interactions. Consequently, the optimization process had to discover the nature of these links. We find that sts₄₄₅ correctly recovered the excitatory and inhibitory checkerboard pattern of ePT → lPT interactions, matching the ground truth in both sign and relative magnitude (compare Figure 6a versus Figure 6c).

To analyze the fidelity of dynamic mechanisms of the discovered models, we performed an impulse response analysis (Appendix C.2), perturbing the system to a saturated state and observing the relaxation dynamics under different behavioral contexts (swimming versus resting): While ts₄₂₂ produces spurious oscillations and fails to capture the correct decay rates, sts₄₄₅ closely tracks the ground truth trajectories as shown in Figure S2.

We confirm the qualitative differences discussed in this section by quantitative metrics reported in Table S1: We find that, relative to ts₄₂₂, sts₄₄₅ achieves a more than 30-fold reduction in effective connectivity error (\mathcal{L}_{Jac}), and a more than 5-fold reduction in impulse response error (\mathcal{L}_{IR}). Table S2 reports the same metrics for the top 50 highest-scoring solutions of both tree searches, confirming the robustness of these results.

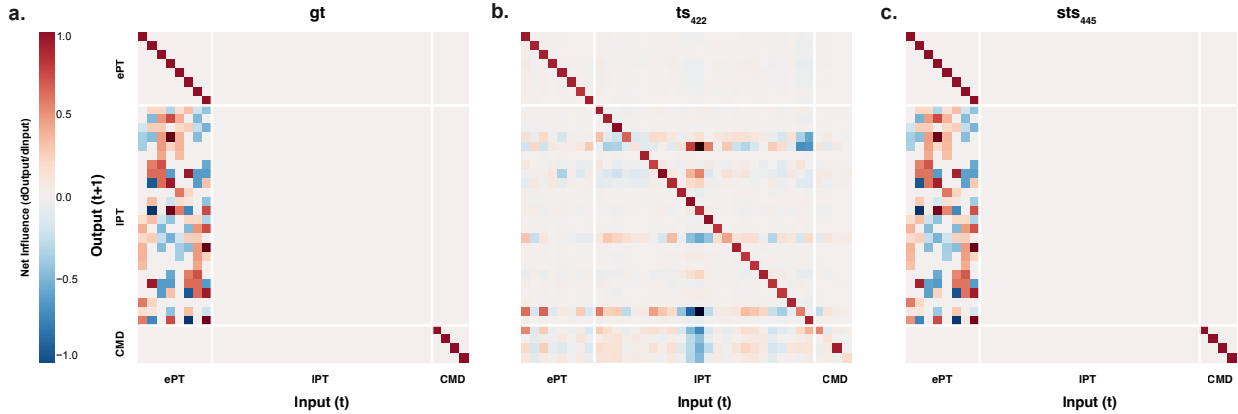


Figure 6 | Structural priors enable mechanistic recovery. **a.** Effective connectivity matrices derived via Jacobian sensitivity analysis for the ground-truth circuit. Note the distinct excitatory (red) and inhibitory (blue) pattern in the ePT → IPT interactions (middle-left block) and the absence of recurrence in the IPT block (center). **b.** The unconstrained ts_{422} model largely fails to capture the ePT → IPT interactions, instead relying on spurious recurrent IPT dynamics. **c.** The structure-constrained model, which received a boolean mask for ePT → IPT connectivity but no information about strength, faithfully recovers the sign and magnitude pattern of the interactions.

Taken together, these analyses show that structural priors enable the discovery of models that abandon statistical shortcuts in favor of recovering true mechanisms, allowing faithful system identification.

4. Discussion

Our analysis reveals that sensory drive is a prerequisite for identifiability, while in-distribution accuracy is a poor proxy for system identification. Crucially, we find that structural priors enable mechanistic recovery, eliminating statistical shortcuts that unconstrained models exploit. These insights motivate three concrete recommendations for future modeling of real-world datasets:

#1: Redefining prediction tasks. Current benchmarks, such as ZAPBench (Lueckmann et al., 2025) which is based on whole-brain neural activity recordings from a larval zebrafish, treat neural activity as a self-contained time series suitable for autoregressive prediction. However, our control experiments show that without access to the driving sensory signals, the true circuit mechanisms may be non-identifiable. In real-world recordings, this issue is exacerbated by additional unobserved drivers (e.g., olfactory, auditory, or mechanosensory inputs). We propose changing the task from predicting future activity from history and stimulus to predicting downstream integration, conditioned on the activity of sensory populations identified via the connectome.

#2: OOD generalization as the primary metric. We show that unconstrained models can achieve near-perfect accuracy on familiar data by exploiting statistical shortcuts, only to fail completely when the stimulus changes. To ensure models capture true mechanisms rather than dataset-specific correlations, evaluation should prioritize performance on held-out stimulus classes or perturbation studies.

#3: Use physical wiring as a scaffold. We propose a shift toward structural grey-box modeling. While black-box models currently dominate neural forecasting, our *in silico* experiments suggest they poorly recover mechanisms and tend to have limited interpretability.

The upcoming release of the synapse-resolution connectome for the ZAPBench specimen will make

these recommendations practical and offer an opportunity to test a key result from our work: that static wiring diagrams can serve as potent scaffold. It is often assumed that recovering mechanisms requires detailed knowledge of synaptic strengths and valences from the ultrastructure or molecular annotations. However, we find that knowing the wiring diagram provides a structural prior that allows an optimization process to infer mechanisms directly from paired neural activity.

Limitations and Future Work. simZFish is a simplification of the vertebrate brain, focusing on a particular visuomotor circuit and associated behavior. Future work could extend the simulator to include broader behavioral repertoires and associated neural circuits. Additionally, while the tree search is applicable to high-dimensional data, the process is computationally intensive. Finally, we prioritized a fully observable, high-fidelity regime to rigorously validate mechanistic recovery against a known ground truth. Extending this to settings with partial observability or lower signal-to-noise ratios is an area for future research.

Conclusion. *In silico* testbeds allow us to better understand the capabilities of AI-driven code search. Our results reveal that treating model discovery purely as an unconstrained error-minimization problem encourages solutions that exploit statistical shortcuts rather than faithful system identification. As we deploy these tools on complex real-world science problems, testbeds with verifiable solutions can guide the design of constraints and metrics needed to align AI-driven discovery with scientific utility and mechanistic understanding.

Acknowledgements

We would like to thank Peter H. Li, Franz Rieger, Zhengdao Chen, and the Science AI team at Google Research for discussions and project support. We also thank the authors of open-source software enabling this work, including simZFish (Liu et al., 2025), Webots (Michel, 2004), JAX (Bradbury et al., 2018), Flax (Heek et al., 2024), and the wider Python community.

References

E. Aygün, A. Belyaeva, G. Comanici, M. Coram, H. Cui, J. Garrison, R. J. A. Kast, C. Y. McLean, P. Norgaard, Z. Shamsi, D. Smalling, J. Thompson, S. Venugopalan, B. P. Williams, C. He, S. Martinson, M. Plomecka, L. Wei, Y. Zhou, Q.-Z. Zhu, M. Abraham, E. Brand, A. Bulanova, J. A. Cardille, C. Co, S. Ellsworth, G. Joseph, M. Kane, R. Krueger, J. Kartiwa, D. Liebling, J.-M. Lueckmann, P. Raccuglia, X. Wang, K. Chou, J. Manyika, Y. Matias, J. C. Platt, L. Dorfman, S. Mourad, and M. P. Brenner. An AI system to help scientists write expert-level empirical software. *arXiv preprint*, 2025. URL <https://doi.org/10.48550/arXiv.2509.06503>.

J. Bradbury, R. Frostig, P. Hawkins, M. J. Johnson, C. Leary, D. Maclaurin, G. Necula, A. Paszke, J. VanderPlas, S. Wanderman-Milne, and Q. Zhang. JAX: Composable transformations of Python+NumPy programs, 2018. URL <https://github.com/jax-ml/jax>.

S.-A. Chen, C.-L. Li, N. Yoder, S. O. Arik, and T. Pfister. TSMixer: An all-MLP architecture for time series forecasting. *Transactions on Machine Learning Research*, 2023. URL <https://openreview.net/forum?id=wbpXTuXgm0>.

X. Chen, Y. Mu, Y. Hu, A. T. Kuan, M. Nikitchenko, O. Randlett, A. B. Chen, J. P. Gavornik, H. Sompolinsky, F. Engert, and M. B. Ahrens. Brain-wide organization of neuronal activity and convergent sensorimotor transformations in larval zebrafish. *Neuron*, 2018. URL <https://doi.org/10.1016/j.neuron.2018.09.042>.

A. Das, W. Kong, A. Leach, S. Mathur, R. Sen, and R. Yu. Long-term forecasting with TiDE. *Transactions on Machine Learning Research*, 2023. URL <https://openreview.net/forum?id=pCbC3aQB5W>.

Google. Gemini 3 Flash: Frontier intelligence built for speed, December 17 2025. URL <https://blog.google/products-and-platforms/products/gemini/gemini-3-flash/>. The Keyword.

J. Heek, A. Levskaya, A. Oliver, M. Ritter, B. Rondepierre, A. Steiner, and M. van Zee. Flax: A neural network library and ecosystem for JAX, 2024. URL <https://github.com/google/flax>.

X. Liu, M. D. Loring, L. Zunino, K. E. Fouke, F. A. Longchamp, A. Bernardino, A. J. Ijspeert, and E. A. Naumann. Artificial embodied circuits uncover neural architectures of vertebrate visuomotor behaviors. *Science Robotics*, 2025. URL <https://doi.org/10.1126/scirobotics.adv4408>.

L. Ljung. Perspectives on system identification. *Annual Reviews in Control*, 2010. URL <https://doi.org/10.1016/j.arcontrol.2009.12.001>.

J.-M. Lueckmann, A. Immer, A. B.-Y. Chen, P. H. Li, M. D. Petkova, N. A. Iyer, L. W. Hesselink, A. Dev, G. Ihrke, W. Park, A. Petruccio, A. Weigel, W. Korff, F. Engert, J. Lichtman, M. Ahrens, M. Januszewski, and V. Jain. ZAPBench: A benchmark for whole-brain activity prediction in zebrafish. In *International Conference on Learning Representations*, 2025. URL <https://openreview.net/forum?id=oCHsDpyawq>.

O. Michel. Webots: Professional mobile robot simulation. *Journal of Advanced Robotics Systems*, 2004. URL <https://doi.org/10.5772/5618>.

F. Pei, J. Ye, D. Zoltowski, A. Wu, R. H. Chowdhury, H. Sohn, J. E. O'Doherty, K. V. Shenoy, M. T. Kaufman, M. Churchland, M. Jazayeri, L. E. Miller, J. Pillow, I. M. Park, E. L. Dyer, and C. Pandarinath. Neural Latents Benchmark '21: Evaluating latent variable models of neural population activity. In *NeurIPS*, 2021. URL <https://doi.org/10.48550/arXiv.2109.04463>.

D. Salinas, V. Flunkert, J. Gasthaus, and T. Januschowski. Deepar: Probabilistic forecasting with autoregressive recurrent networks. *International Journal of Forecasting*, 2020. URL <https://doi.org/10.1016/j.ijforecast.2019.07.001>.

M. Schrimpf, J. Kubilius, M. J. Lee, N. A. R. Murty, R. Ajemian, and J. J. DiCarlo. Integrative Benchmarking to Advance Neurally Mechanistic Models of Human Intelligence. *Neuron*, 2020. URL <https://doi.org/10.1016/j.neuron.2020.07.040>.

D. Silver, A. Huang, C. J. Maddison, A. Guez, L. Sifre, G. van den Driessche, J. Schrittwieser, I. Antonoglou, V. Panneershelvam, M. Lanctot, S. Dieleman, D. Grewe, J. Nham, N. Kalchbrenner, I. Sutskever, T. Lillicrap, M. Leach, K. Kavukcuoglu, T. Graepel, and D. Hassabis. Mastering the game of Go with deep neural networks and tree search. *Nature*, 2016. URL <https://doi.org/10.1038/nature16961>.

C. Sourmpis, C. C. Petersen, W. Gerstner, and G. Bellec. Biologically informed cortical models predict optogenetic perturbations. *eLife*, 2025. URL <https://doi.org/10.7554/eLife.106827.2>.

P. Turishcheva, P. G. Fahey, L. Hansel, R. Froebe, K. Ponder, M. Vystrčilová, K. F. Willeke, M. Bashiri, E. Wang, Z. Ding, A. S. Tolias, F. H. Sinz, and A. S. Ecker. The dynamic sensorium competition for predicting large-scale mouse visual cortex activity from videos. *arXiv preprint*, 2023. URL <https://doi.org/10.48550/arXiv.2305.19654>.

P. Vahidi, O. G. Sani, and M. M. Shanechi. Modeling and dissociation of intrinsic and input-driven neural population dynamics underlying behavior. *Proceedings of the National Academy of Sciences*, 2024. URL <https://doi.org/10.1073/pnas.2212887121>.

A. Zeng, M. Chen, L. Zhang, and Q. Xu. Are transformers effective for time series forecasting? In *AAAI Conference on Artificial Intelligence*, 2023. URL <https://doi.org/10.1609/aaai.v37i9.26317>.

Appendices

A	Related Work	2
B	Neuromechanical Simulations	3
C	Additional Analyses	5
C.1	Effective Connectivity Analysis	5
C.2	Impulse Response Analysis	5
D	Baseline Models	6
D.1	mean	6
D.2	nlinear	6
D.3	tide	6
D.4	tsmixer	6
D.5	depar	6
E	Tree Search	7
E.1	Search Algorithm	7
E.2	Implementation Details	7
E.3	Prompts	7
F	Code Listings	10
F.1	Initial Code for Tree Search	10
F.2	Solution ts_{001}	11
F.3	Solution ts_{422}	12
F.4	Solution sts_{445}	14
G	Supplementary Figures	17
H	Supplementary Tables	19
	References	20

A. Related Work

Automated Model Discovery. Our work uses the capability of Large Language Models (LLMs) to perform automated model discovery via code generation. While traditional approaches to model discovery relied on genetic programming (Schmidt and Lipson, 2009) or reinforcement learning for neural architecture search (Zoph and Le, 2017), recent methods treat the search process as an evolution of executable code. We utilize the tree-search methodology proposed by Aygün et al. (2025). Parallel efforts have explored similar LLM-driven evolutionary strategies for mathematical discovery (Romera-Paredes et al., 2024) and algorithmic evolution (Novikov et al., 2025; Lange et al., 2025; Jiang et al., 2025). In related domains, automated model discovery techniques have for example been applied to search for interpretable cognitive models of human and animal behavior (Castro et al., 2025), and neural tuning curves (Tilbury et al., 2025). Our work distinguishes itself by applying these methods to neural system identification in a setting where we can rigorously benchmark the discovery of mechanisms against a verifiable ground truth.

System Identification with Ground Truth. The difficulty of inferring ground-truth mechanisms from neural data is a long-standing methodological concern. Jonas and Kording (2017) utilized a microprocessor to demonstrate that standard data analysis techniques can fail to recover the known logic of information processing. More recently, Han et al. (2023) used artificial neural networks (ANNs) as *in silico* ground truths, revealing that functional similarity (predictive performance) does not imply mechanistic similarity. We advance this line of inquiry by moving beyond artificial proxies—such as microprocessors or generic ANNs—which differ fundamentally from biological substrates. Instead, we employ a high-fidelity, experimentally constrained emulation of the zebrafish optomotor response to move towards more realistic models with ground truth.

Neuromechanical Simulations and Connectome Constraints. Our work is situated within the growing field of neuromechanical modeling. While detailed simulations have been established for invertebrates such as the worm *C. elegans* (Sarma et al., 2018; Zhao et al., 2024) and the fruit fly *D. melanogaster* (Lobato-Rios et al., 2022; Vaxenburg et al., 2025), we utilize a larval zebrafish simulation to capture vertebrate visuomotor dynamics. Concurrently, the increasing availability of connectomes has spurred research into constraining neural models with physical wiring diagrams. The success of our structurally constrained models aligns with the findings of Sourmpis et al. (2025), who demonstrated that biologically informed models are more robust to optogenetic perturbations than generic RNNs. Several studies, including Mi et al. (2021); Achterberg et al. (2023); Lappalainen et al. (2024); Beiran and Litwin-Kumar (2025); Duan et al. (2025), have highlighted the predictive utility of structural constraints. Our work bridges these findings with automated discovery: rather than manually designing constrained architectures, we show that connectomic information can be used with AI-driven search to navigate the vast space of possible models and recover mechanistic solutions.

B. Neuromechanical Simulations

We detail the numerical values for the parameters introduced in the neural circuit model (Section 2.1), which are based on the reference implementation [Liu et al. \(2025\)](#).

Early Precortex (ePT). The ePT dynamics described in [Equation 2](#) are governed by the update rate α_t and the response function parameters $\omega_{\text{ept}}, \mathbf{b}_{\text{ept}}$:

$$\alpha_t = \begin{cases} 0.002 & \text{if swim bout active,} \\ 0.01 & \text{otherwise,} \end{cases}$$

$$\omega_{\text{ept}} = [0.068, 0.100, 0.068, 0.100, 0.068, 0.100, 0.068, 0.100]^\top,$$

$$\mathbf{b}_{\text{ept}} = [90.0, 60.0, 90.0, 60.0, 90.0, 60.0, 90.0, 60.0]^\top.$$

The ePT state vector is ordered as $\mathbf{h}^{\text{ept}} = [\text{ePT}_L^S, \text{ePT}_L^A, \text{ePT}_L^I, \text{ePT}_L^P, \text{ePT}_R^S, \text{ePT}_R^A, \text{ePT}_R^I, \text{ePT}_R^P]^\top$, i.e., grouped by hemisphere (Left, Right) and functional tuning (Superior, Anterior, Inferior, Posterior).

Late Precortex (lPT). The lPT activations in [Equation 3](#) are computed using the connectivity matrix \mathbf{W}_{lpt} , the gating mask \mathbf{M}_{gate} , and response parameters $\omega_{\text{lpt}}, \mathbf{b}_{\text{lpt}} \in \mathbb{R}^{24}$:

$$\mathbf{W}_{\text{lpt}} = \begin{bmatrix} 0 & 1 & 1 & -1.5 & 0.8 & 1.5 & -1 & -2 \\ 0 & -1 & 1 & 1.5 & 0.8 & 0 & -1 & 0 \\ -0.8 & 1 & 1 & 0 & 0.8 & 1 & -1 & -2 \\ -0.8 & -1 & 1 & 2.5 & 0.8 & 0 & -1 & 0 \\ -0.8 & 0 & 1 & 0.5 & 0.8 & 0 & 0 & 0 \\ 0 & 0 & 1 & 0 & 0.8 & 0 & 0 & 0 \\ 0 & 0.8 & 1 & 0 & 0 & 0 & 0 & -0.8 \\ 0 & 1 & 1 & -1 & 0 & 1.5 & -1 & -1 \\ 0 & -1.5 & 1 & 1.5 & 0 & 0 & -1 & 0.5 \\ 0 & 0 & 0 & 0.8 & 0.3 & 0.3 & 0 & 0 \\ 0 & 1.5 & 1 & -1 & 0.8 & 0.5 & 0 & -2 \\ 0 & -1.5 & 1 & 1.5 & 0.8 & -1 & 0 & 1 \\ 0.8 & 1.5 & -1 & -2 & 0 & 1 & 1 & -1.5 \\ 0.8 & 0 & -1 & 0 & 0 & -1 & 1 & 1.5 \\ 0.8 & 1 & -1 & -2 & -0.8 & 1 & 1 & 0 \\ 0.8 & 0 & -1 & 0 & -0.8 & -1 & 1 & 2.5 \\ 0.8 & 0 & 0 & 0 & -0.8 & 0 & 1 & 0.5 \\ 0.8 & 0 & 0 & 0 & 0 & 0 & 1 & 0 \\ 0 & 0 & 0 & -0.8 & 0 & 0.8 & 1 & 0 \\ 0 & 1.5 & -1 & -1 & 0 & 1 & 1 & -1 \\ 0 & 0 & -1 & 0.5 & 0 & -1.5 & 1 & 1.5 \\ 0.8 & 0.3 & 0 & 0 & 0 & 0 & 0 & 0 \\ 0.8 & 0.5 & 0 & -2 & 0 & 1.5 & 1 & -1 \\ 0.8 & -1 & 0 & 1 & 0 & -1.5 & 1 & 1.5 \end{bmatrix}, \quad \mathbf{M}_{\text{gate}} = \begin{bmatrix} 0 \\ 0 \\ 0 \\ 0 \\ 0 \\ 0 \\ 1 \\ 1 \\ 0 \\ 0 \\ 0 \\ 0 \\ 0 \\ 0 \\ 0 \\ 0 \\ 0 \\ 0 \\ 0 \\ 0 \\ 1 \\ 1 \\ 1 \\ 1 \end{bmatrix}, \quad \omega_{\text{lpt}} = \begin{bmatrix} 2.5 \\ 2.5 \\ 2.5 \\ 2.5 \\ 2.5 \\ 2.5 \\ 4.0 \\ 4.0 \\ 4.0 \\ 4.0 \\ 5.0 \\ 4.0 \\ 4.0 \\ 4.0 \\ 4.0 \\ 4.0 \\ 4.0 \\ 4.0 \\ 4.0 \\ 4.0 \\ 4.0 \\ 4.0 \\ 4.0 \\ 4.0 \\ 4.0 \end{bmatrix}, \quad \mathbf{b}_{\text{lpt}} = \begin{bmatrix} 0.8 \\ 0.8 \\ 0.8 \\ 0.8 \\ 0.8 \\ 0.8 \\ 0.6 \\ 0.6 \\ 0.6 \\ 0.6 \\ 0.4 \\ 0.6 \\ 0.6 \\ 0.6 \\ 0.6 \\ 0.6 \\ 0.6 \\ 0.6 \\ 0.6 \\ 0.6 \\ 0.6 \\ 0.6 \\ 0.6 \\ 0.6 \\ 0.6 \\ 0.6 \end{bmatrix}.$$

The lPT state vector is ordered as

$$\mathbf{h}^{\text{lpt}} = [\text{lPT}_L^{\text{OB}1}, \text{lPT}_L^{\text{OB}2}, \text{lPT}_L^{\text{B}1}, \text{lPT}_L^{\text{B}2}, \text{lPT}_L^{\text{iB}}, \text{lPT}_L^{\text{ioB}}, \text{lPT}_L^{\text{iMm}}, \text{lPT}_L^{\text{Mm}1}, \text{lPT}_L^{\text{Mm}2}, \text{lPT}_L^{\text{oMm}}, \text{lPT}_L^{\text{S}1}, \text{lPT}_L^{\text{S}2}, \text{lPT}_R^{\text{OB}1}, \dots, \text{lPT}_R^{\text{S}2}]^\top,$$

grouping first by hemisphere (Left, Right) and then by functional type.

The gating function $\mathbf{g}(\mathbf{h})$ referenced in [Equation 3](#) implements a “soft” AND-gate using a minimum operation between specific pairs of inputs. This function selects specific ipsilateral (\mathbf{h}^{ipsi}) and contralateral ($\mathbf{h}^{\text{contra}}$) components from the ePT state vector \mathbf{h}^{ept} . Specifically, for “S-type”-LPT neurons, the gating signal requires activation from both contralateral Superior and ipsilateral Inferior inputs:

$$\mathbf{g}(\mathbf{h}) = \min(0.8 \cdot \mathbf{h}^{\text{contra}}, \mathbf{h}^{\text{ipsi}}) = \min(0.8 \cdot \text{ePT}_R^S, \text{ePT}_L^I).$$

This ensures the neuron is only active when both specific directional conditions are met, scaled by a factor of 0.8 on the contralateral input to account for asymmetric drive.

Command Neurons (nMLF/aHB). The dynamics of the command neurons in [Equation 4](#) are defined by the update rate $\beta = 0.0005$, connectivity \mathbf{W}_{cmd} , and response parameters ω_{cmd} , \mathbf{b}_{cmd} :

$$\mathbf{W}_{\text{cmd}}^{1\dots 12} = \begin{bmatrix} 0.1 & -0.1 & 0.32 & -0.08 & 0.25 & -0.05 & 0.6 & 0.4 & 0 & 0 & 0.3 & -0.1 \\ 0 & 0 & 0 & 0 & 0 & 0 & 0 & 0 & 0 & -0.8 & 0 & 0 \\ 0.1875 & 0.3875 & 0.2165 & 0.3165 & 0 & 0 & 0 & 0.0165 & 0.4165 & 0 & 0.096 & 0.096 \\ -0.1665 & -0.1665 & -0.1665 & -0.1665 & 0 & 0 & 0 & -0.105 & -0.105 & 0 & -0.29 & -0.29 \end{bmatrix},$$

$$\mathbf{W}_{\text{cmd}}^{13\dots 24} = \begin{bmatrix} 0 & 0 & 0 & 0 & 0 & 0 & 0 & 0 & 0 & -0.8 & 0 & 0 \\ 0.1 & -0.1 & 0.32 & -0.08 & 0.25 & -0.05 & 0.6 & 0.4 & 0 & 0 & 0.3 & -0.1 \\ -0.1665 & -0.1665 & -0.1665 & -0.1665 & 0 & 0 & 0 & -0.105 & -0.105 & 0 & -0.29 & -0.29 \\ 0.1875 & 0.3875 & 0.2165 & 0.3165 & 0 & 0 & 0 & 0.0165 & 0.4165 & 0 & 0.096 & 0.096 \end{bmatrix},$$

$$\omega_{\text{cmd}} = [6.5, 6.5, 4.0, 4.0]^\top, \quad \mathbf{b}_{\text{cmd}} = [0.4, 0.4, 0.65, 0.65]^\top.$$

The resulting command state vector is ordered as $\mathbf{h}_t^{\text{cmd}} = [\text{nMLF}_L, \text{nMLF}_R, \text{aHB}_L, \text{aHB}_R]^\top$.

Motor circuits. The evidence accumulation dynamics in [Equation 5](#) are defined by the integrator threshold $\theta = 436.0$, noise standard deviation $\sigma = 0.65$, and nMLF input scaling factor $\gamma = 0.6$.

The action probabilities defined in [Equation 6](#) are computed using the command state vector $\mathbf{h}_t^{\text{cmd}}$, the projection matrix \mathbf{W}_{act} , and \mathbf{b}_{act} :

$$\mathbf{W}_{\text{act}} = \begin{bmatrix} 1 & 1 & 0 & 0 \\ 0 & 0 & 1 & 0 \\ 0 & 0 & 0 & 1 \end{bmatrix}, \quad \mathbf{b}_{\text{act}} = \begin{bmatrix} 0.200 \\ 0.066 \\ 0.066 \end{bmatrix}.$$

For an explanation of all other stages in the model, see [Liu et al. \(2025\)](#).

C. Additional Analyses

C.1. Effective Connectivity Analysis

To evaluate whether the discovered models recover the true static mechanisms of the neural circuit, we computed the *Effective Connectivity Matrix*. This matrix quantifies the sensitivity of the predicted neural state at time $t + 1$ to perturbations in the state at time t (Figure 6).

Formally, we analyze the one-step transition $\mathbf{a}_{t+1} = f_\theta(\mathbf{a}_t, \mathbf{x}_{t+1})$. The effective connectivity matrix $J \in \mathbb{R}^{N \times N}$ is defined as the Jacobian of the future state with respect to the current state:

$$J_{ij} = \frac{\partial(\mathbf{a}_{t+1})_i}{\partial(\mathbf{a}_t)_j} \quad (\text{S1})$$

where J_{ij} represents the causal influence of source neuron j on target neuron i .

To isolate the intrinsic connectivity of the circuit, we compute J while setting exogenous covariates to zero ($\mathbf{x}_{t+1} = \mathbf{0}$). To account for non-linearities (e.g., sigmoids) where gradients vanish in saturated regions, we do not evaluate J at a single operating point. Instead, we estimate the expected sensitivity by averaging over $K = 11$ homogeneous probe states. We define a set of scalars $\mathcal{S} = \{0.0, 0.1, \dots, 1.0\}$ and construct input vectors $\mathbf{a}^{(s)} = s \cdot \mathbf{1}$, where $\mathbf{1}$ is the all-ones vector. The reported connectivity is:

$$\bar{J} = \frac{1}{|\mathcal{S}|} \sum_{s \in \mathcal{S}} J|_{\mathbf{a}_t=\mathbf{a}^{(s)}} \quad (\text{S2})$$

We quantify the mechanistic fidelity of a model by comparing its connectivity \bar{J}_{model} to the ground truth \bar{J}_{gt} using the Frobenius norm:

$$\mathcal{L}_{\text{jac}} = \|\bar{J}_{\text{model}} - \bar{J}_{\text{gt}}\|_F \quad (\text{S3})$$

C.2. Impulse Response Analysis

To assess recovery of dynamic mechanisms, we performed an *Impulse Response Analysis*. We probe how the system relaxes from perturbed states back to rest, and how this dynamic is modulated by behavioral states.

We simulate the system for a horizon of $H = 256$ steps starting from a set of impulse conditions. We test $N + 1$ initial conditions: 36 cases where a single neuron is activated ($\mathbf{a}_0 = \mathbf{e}_i$) and one case where the entire system is saturated ($\mathbf{a}_0 = \mathbf{1}$). We evolve these states using two fixed covariates \mathbf{x}_{mode} to test mechanisms depending on swim state (e.g., the ePT update in Equation 2):

1. **Rest:** Bout state and sensory drive set to 0.
2. **Swim:** Bout state set to 1, sensory drive set to 0.

We quantify the divergence between the model's predicted response traces ($\hat{\mathbf{A}}$) and the ground truth traces (\mathbf{A}^*) using the Mean Absolute Error (MAE) averaged over all time steps, units, and initial conditions. We report this metric separately for the two regimes:

$$\mathcal{L}_{\text{IR}}^{\text{rest}} = \text{MAE}(\hat{\mathbf{A}}^{\text{rest}}, \mathbf{A}^{\text{rest}}), \quad \mathcal{L}_{\text{IR}}^{\text{swim}} = \text{MAE}(\hat{\mathbf{A}}^{\text{swim}}, \mathbf{A}^{\text{swim}}) \quad (\text{S4})$$

D. Baseline Models

D.1. `mean`

The naive `mean` baseline repeats the per-neuron activity from the last timestep across the entire prediction horizon.

D.2. `nlinear`

For `nlinear` (Zeng et al., 2023), we use a model with context window size of 2. For optimization, we use AdamW (Loshchilov and Hutter, 2019) with a learning rate of 10^{-4} and weight decay of 10^{-4} .

D.3. `tide`

For `tide` (Das et al., 2023), we use a model with a context window size of 2, 2 encoder and decoder layers each, a hidden layer size of 128, a decoder output dimensionality of 32, and reversible instance norm. For optimization, we use AdamW (Loshchilov and Hutter, 2019) with a learning rate of 10^{-3} and weight decay of 10^{-4} .

D.4. `tsmixer`

For `tsmixer` (Chen et al., 2023), we use a model with a context window size of 2, 2 blocks, and an MLP dimension of 256, and no instance norm. For optimization, we use AdamW (Loshchilov and Hutter, 2019) with a learning rate of 10^{-3} and weight decay of 10^{-4} .

D.5. `deepar`

For `deepar` (Salinas et al., 2020), we use a model with 2 stacked GRU layers, with a hidden size of 128. For optimization, we use AdamW (Loshchilov and Hutter, 2019) with a learning rate of 10^{-3} and weight decay of 10^{-4} .

E. Tree Search

We formulate the model discovery process as a search problem where the state space consists of executable Python code defining neural transition functions, and the objective is to maximize predictive accuracy on the validation set.

E.1. Search Algorithm

We utilize the Predictor Upper Confidence Bound applied to Trees (PUCT) algorithm (Silver et al., 2016; Aygün et al., 2025) to balance exploration of novel solutions and exploitation (refining high-performing solutions). Unlike standard Monte Carlo Tree Search, where the algorithm traverses from the root to a leaf node for expansion, the space of possible code edits here is effectively infinite. Consequently, the algorithm treats every existing node in the tree as a candidate for expansion.

At each step, a node u^* is sampled from the entire tree \mathcal{T} by maximizing the PUCT objective:

$$u^* = \operatorname{argmax}_{u \in \mathcal{T}} \left(\tilde{R}(u) + c_{\text{puct}} |\mathcal{T}|^{-1} \frac{\sqrt{\sum_{v \in \mathcal{T}} V(v)}}{1 + V(u)} \right), \quad (\text{S5})$$

where $V(u)$ is the visit count of node u , c_{puct} is an exploration constant, and $|\mathcal{T}|^{-1}$ acts as a flat prior.

The term $\tilde{R}(u)$ represents the normalized rank score of a solution. Solutions are scored by calculating the negative Mean Absolute Error (MAE) on the validation set, averaged over in-distribution conditions. These raw scores are converted into ranks $\text{Rank}_{\mathcal{T}}(u)$ in ascending order (where the best solution with the least error has the highest rank), and normalized as:

$$\tilde{R}(u) = \frac{\text{Rank}_{\mathcal{T}}(u) - 1}{|\mathcal{T}| - 1}. \quad (\text{S6})$$

Upon selecting a node u^* , we prompt the LLM to generate a child node by modifying the source code of u^* . The LLM acts as a mutation operator, guided by instructions defined in Appendix E.3, and the initial code specified in Appendix F.1. The generated code is immediately executed in a sandboxed environment to compute the validation score on the task defined in the Section 2.2.1. Finally, the visit count V is incremented for the selected node and backpropagated to its ancestors.

E.2. Implementation Details

We utilized Gemini 3 Flash (Google, 2025) as the backbone LLM for code generation and mutation. Each tree search was limited to a maximum of 500 nodes. To ensure computational feasibility on a single NVIDIA T4 GPU, we enforced a runtime limit of 12 hours per candidate solution. To further accelerate the discovery process, we employed a truncated training regime: models were trained on a short rollout of 32 timesteps. We found this efficient training proxy sufficient to identify architectures that generalize well when rolled out to the full prediction horizon (256 timesteps) used for scoring and evaluation.

E.3. Prompts

The initial prompt for tree search, without prior information about structure:

```

# Predicting neural activity

## Challenge

Your task is to build a forecasting model that **predicts future neural activity traces given past activity and covariates**.

**Data Specifications:**
- **Inputs & Outputs:** All neural activity and continuous covariates are normalized to the [0, 1] range.
- **Covariates (cov_t):** Shape (Batch, CovFeatures=9).
  - cov_t[..., 0]: **Bout State**. A binary flag (0 or 1). This acts as a switch for the system's dynamics.
  - cov_t[..., 1:]: **Visual Input**. Continuous signals [0, 1] driving the system.

**Key Difficulties:**
1. **Autoregressive Stability:** You will develop a transition model  $f(y_{t-1}, c_t) \rightarrow y_t$ . This is rolled out for 32 timesteps. Small errors at step 1 can explode by step 32.
2. **OOD Generalization:** The test set contains visual patterns **not seen during training**. Your model must capture the underlying causal rules, not memorize training sequences.

## Evaluation

Performance is measured by Mean Absolute Error (MAE) on held-out trajectories. Lower is better.

## Rules

1. **Structure:** Keep the sections 'CONSTANTS', 'MODEL', and 'OPTIMIZER' in this order.
2. **Interface - Hyperparameters:** You **must** define the following constants in the 'CONSTANTS' section to control the training harness:
  * 'BATCH_SIZE': (int) Default ~512.
  * 'MAX_STEPS': (int) Default ~500,000.
  * 'SCHEDULED_SAMPLING_START_PROB' & 'SCHEDULED_SAMPLING_FINAL_PROB': (float) Controls teacher forcing. High start (1.0) helps convergence; low final (<0.1) enforces stability.
  * 'SCHEDULED_SAMPLING_DECAY_STEPS': (int) Steps to decay the probability.
  * 'EARLY_STOP_PATIENCE': (int) Steps to wait before stopping.
  * 'MIN_DELTA': (float) Improvement threshold for early stopping.
3. **Interface - Model:** 
  - Use 'flax.linen'. Class name must be 'Candidate'.
  - '__call__' signature: '(self, past_pred, cov_t, train=False)'.
  - **Shape Contract:** Input 'past_pred' is (B, 36). Output must be (B, 36).
4. **Interface - Optimizer:** 
  - Use 'optax'. Instance must be named 'optimizer'.
5. **Constraints:** Do not modify code in 'NOTE' comments.

## Strategic Approaches & Hints

To win this competition, you should explore distinct architectural ideas. Do not limit yourself to simple MLPs.

```

For the tree search with structural prior, the **Strategic Approaches & Hints** section in the prompt was extended as follows:

We have prior knowledge about the neuron hierarchy that is likely critical for a low score. The 36 neurons are split into three groups with specific dependencies:

- **EPT Neurons (Indices 0-8):** Depend on their past state (`'past_pred[..., 0:8]'`) and current covariates (`'cov_t'`). The bout state `'cov_t[..., 0]` acts as a switch, modulating the neurons' update dynamics based on whether a bout is active. Each neuron i in this group (indices 0-7) is driven by a specific visual input: `'cov_t[..., 1+i]` (e.g., neuron 0 depends on `'cov_t[..., 1]`, neuron 1 on `'cov_t[..., 2]`, and so on).
- **LPT Neurons (Indices 8:32):** Depend only on the **newly computed EPT activations** (current step's neurons 0-7), not on their own past activations from `past_pred`. The `'CONNECTIVITY'` variable below indicates sparse connections: `'CONNECTIVITY[i][j]` is true if the i -th neuron within the EPT group depends on the j -th neuron within the LPT group. Since i ranges from 0-23 and j from 0-7, `'CONNECTIVITY[0][j]` refers to dependencies of neuron 8 (first LPT neuron), `'CONNECTIVITY[1][j]` refers to dependencies of neuron 9 (second LPT neuron), and so on.

3. **aHB/nMLF Neurons (Indices 32:36):** Depend on their past state ('`past_pred[..., 32:36]`') and the **newly computed** LPT activations (current step).

... and the following connectivity matrix was included:

```
1 # NOTE: Connectivity from EPT (cols) to LPT (rows)
2 CONNECTIVITY = [
3     [False, True, True, True, True, True, True],
4     [False, True, True, True, True, False, True, False],
5     [True, True, True, False, True, True, True, True],
6     [True, True, True, True, True, False, True, False],
7     [True, False, True, True, True, False, False, False],
8     [False, False, True, False, True, False, False, False],
9     [False, True, True, False, False, False, False, True],
10    [False, True, True, True, False, True, True, True],
11    [False, True, True, True, False, False, True, True],
12    [False, False, False, False, True, True, False, False],
13    [False, True, True, True, True, True, False, True],
14    [False, True, True, True, True, True, False, True],
15    [True, True, True, True, False, True, True, True],
16    [True, False, True, False, False, True, True, True],
17    [True, True, True, True, True, True, True, False],
18    [True, False, True, False, True, True, True, True],
19    [True, False, False, False, True, False, True, True],
20    [True, False, False, False, False, False, True, False],
21    [False, False, False, True, False, True, True, False],
22    [False, True, True, True, False, True, True, True],
23    [False, False, True, True, False, True, True, True],
24    [True, True, False, False, False, False, False, False],
25    [True, True, False, True, False, True, True, True],
26    [True, True, False, True, False, True, True, True]]
```

F. Code Listings

F.1. Initial Code for Tree Search

The initial code, which the tree search was tasked to modify:

```

1  #
2  # CONSTANTS
3  #
4
5  BATCH_SIZE = 512
6  MAX_STEPS = 500_000
7  SCHEDULED_SAMPLING_START_PROB = 1.0
8  SCHEDULED_SAMPLING_FINAL_PROB = 0.01
9  SCHEDULED_SAMPLING_DECAY_STEPS = 100_000
10 EARLY_STOP_PATIENCE = 20
11 MIN_DELTA = 1e-6
12 LEARNING_RATE = 1e-3
13
14
15  #
16  # MODEL
17  #
18
19  class Candidate(nn.Module):
20      """Candidate transition model for neural activity."""
21
22      @nn.compact
23      def __call__(self, past_pred, cov_t, train=False):
24          """
25              Args:
26                  past_pred: (Batch, 36) - Previous neural state [0, 1].
27                  cov_t: (Batch, 9) - Index 0 is Bout {0,1}, 1-8 are Visual [0,1].
28                  train: bool - Training mode flag.
29              Returns:
30                  (Batch, 36) - Predicted next state.
31          """
32          bout_state = cov_t[:, 0:1] # Shape (B, 1)
33          visual_in = cov_t[:, 1:] # Shape (B, 8)
34
35          # TODO: Implement your architecture here.
36
37          # Identity baseline: predicts no change.
38          return past_pred
39
40
41  transition_model = Candidate() # NOTE: Do keep this line as-is.
42
43
44  #
45  # OPTIMIZER
46  #
47
48  optimizer = optax.adamw(learning_rate=LEARNING_RATE, weight_decay=1e-4)

```

F.2. Solution `ts001`

```

1  import jax.numpy as jnp
2  import flax.linen as nn
3  import optax
4
5  #
6  # CONSTANTS
7  #
8
9  BATCH_SIZE = 512
10 MAX_STEPS = 500_000
11 # High start prob uses ground truth; low final prob enforces autoregressive stability.
12 SCHEDULED_SAMPLING_START_PROB = 1.0
13 SCHEDULED_SAMPLING_FINAL_PROB = 0.02
14 SCHEDULED_SAMPLING_DECAY_STEPS = 150_000
15 EARLY_STOP_PATIENCE = 40
16 MIN_DELTA = 1e-6
17 LEARNING_RATE = 1e-3
18
19
20 #
21 # MODEL
22 #
23
24 class Candidate(nn.Module):
25     """Residual transition model for neural activity."""
26
27     @nn.compact
28     def __call__(self, past_pred, cov_t, train=False):
29         """
30             Args:
31                 past_pred: (Batch, 36) - Previous neural state.
32                 cov_t: (Batch, 9) - Bout switch and Visual inputs.
33                 train: bool - Training mode.
34             Returns:
35                 (Batch, 36) - Predicted next state.
36         """
37         # Combine previous state and external drivers
38         # Shape: (Batch, 36 + 9) = (Batch, 45)
39         x = jnp.concatenate([past_pred, cov_t], axis=-1)
40
41         # MLP for state transition dynamics
42         h = nn.Dense(512)(x)
43         h = nn.LayerNorm()(h)
44         h = nn.silu(h)
45
46         h = nn.Dense(512)(h)
47         h = nn.LayerNorm()(h)
48         h = nn.silu(h)
49
50         # Predict the delta (residual). Initialize with zeros so
51         # the model starts as an identity function baseline.
52         delta = nn.Dense(36, kernel_init=nn.initializers.zeros)(h)
53
54         # Autoregressive update: y_t = y_{t-1} + delta
55         next_state = past_pred + delta
56
57         # Ensure valid range [0, 1]
58         return jnp.clip(next_state, 0.0, 1.0)
59
60
61 transition_model = Candidate() # NOTE: Do keep this line as-is.
62
63
64 #
65 # OPTIMIZER

```

```

66 #
67
68 # Learning rate schedule with warmup and cosine decay for stability
69 lr_schedule = optax.warmup_cosine_decay_schedule(
70     init_value=1e-6,
71     peak_value=LEARNING_RATE,
72     warmup_steps=2000,
73     decay_steps=MAX_STEPS,
74 )
75
76 optimizer = optax.adamw(learning_rate=lr_schedule, weight_decay=1e-4)

```

F.3. Solution ts_{422}

```

1 import jax
2 import jax.numpy as jnp
3 import flax.linen as nn
4 import optax
5
6 #
7 # CONSTANTS
8 #
9
10 BATCH_SIZE = 512
11 MAX_STEPS = 500_000
12 # Scheduled sampling enforces autoregressive stability.
13 # We decay slightly slower to allow the model to learn the base rules first.
14 SCHEDULED_SAMPLING_START_PROB = 1.0
15 SCHEDULED_SAMPLING_FINAL_PROB = 0.05
16 SCHEDULED_SAMPLING_DECAY_STEPS = 300_000
17 EARLY_STOP_PATIENCE = 1000
18 MIN_DELTA = 1e-9
19 LEARNING_RATE = 8e-4
20
21 #
22 # MODEL
23 #
24
25 class ResidualBlock(nn.Module):
26     features: int
27
28     @nn.compact
29     def __call__(self, x, context):
30         # Pre-norm architecture for stability
31         norm = nn.LayerNorm()(x)
32
33         # Gated Linear Unit (GEGLU variant)
34         # Use context to modulate the hidden representation
35         h = nn.Dense(self.features * 2, kernel_init=nn.initializers.orthogonal())(norm)
36         h_val, h_gate = jnp.split(h, 2, axis=-1)
37         h = h_val * nn.gelu(h_gate)
38
39         # FiLM modulation using context
40         gamma = nn.Dense(self.features, kernel_init=nn.initializers.zeros)(context)
41         beta = nn.Dense(self.features, kernel_init=nn.initializers.zeros)(context)
42         h = h * (1.0 + gamma) + beta
43
44         h = nn.Dense(self.features, kernel_init=nn.initializers.orthogonal()(h)
45         return x + h
46
47 class Candidate(nn.Module):
48     """
49     Refined Gated Dynamics Model.

```

```

50     Models neural transitions using learned time-constants and target states,
51     heavily conditioned on the behavioral 'Bout' switch.
52     """
53
54     @nn.compact
55     def __call__(self, past_pred, cov_t, train=False):
56         B, N = past_pred.shape # N=36
57
58         # 1. Input Processing
59         # Split covariates: Bout State (switch) and Visual Input (driving signal)
60         bout = cov_t[:, 0:1]
61         visual = cov_t[:, 1:]
62
63         # High-dimensional visual embedding
64         v_enc = nn.Dense(128)(visual)
65         v_enc = nn.gelu(v_enc)
66
67         # Context incorporates the Bout switch explicitly
68         # We use the bout flag to gate visual information
69         ctx = jnp.concatenate([
70             v_enc,
71             bout,
72             v_enc * bout, # Bout-specific visual processing
73             v_enc * (1.0 - bout) # Non-bout specific visual processing
74         ], axis=-1)
75         ctx = nn.Dense(128)(ctx)
76         ctx = nn.gelu(ctx)
77
78         # 2. Latent Projection
79         # Project current neural state to a latent space
80         latent_dim = 256
81         x = nn.Dense(latent_dim, kernel_init=nn.initializers.orthogonal())(past_pred)
82
83         # Apply N residual blocks with conditional modulation
84         for i in range(3):
85             x = ResidualBlock(features=latent_dim, name=f"res_block_{i}")(x, ctx)
86
87         # 3. Liquid-Style Transition
88         # We predict a 'gate' (alpha) and a 'target' state.
89         # This ensures the output is always a convex combination of previous state
90         # and a target, guaranteeing stability in [0, 1].
91
92         # Gate: How much the state changes (1/tau)
93         # We initialize it to be small to favor stability early on
94         gate_logit = nn.Dense(N, kernel_init=nn.initializers.zeros()(x))
95         alpha = nn.sigmoid(gate_logit - 3.0)
96
97         # Target: What the neurons are striving towards
98         target = nn.Dense(N, kernel_init=nn.initializers.orthogonal())(x)
99         target = nn.sigmoid(target) # Ensure target is in [0, 1]
100
101         # Direct Delta: Small additive term for fast transient dynamics
102         # This helps capture sudden shifts that a convex combination might miss.
103         delta = nn.Dense(N, kernel_init=nn.initializers.zeros()(x))
104         delta = jnp.tanh(delta) * 0.05
105
106         # Update rule: y_t = (1-alpha)*y_{t-1} + alpha*target + delta
107         next_state = (1.0 - alpha) * past_pred + alpha * target + delta
108
109         return jnp.clip(next_state, 0.0, 1.0)
110
111     transition_model = Candidate() # NOTE: Do keep this line as-is.
112
113     #
114     # OPTIMIZER
115     #
116

```

```

117 lr_schedule = optax.warmup_cosine_decay_schedule(
118     init_value=1e-7,
119     peak_value=LEARNING_RATE,
120     warmup_steps=4000,
121     decay_steps=MAX_STEPS,
122     end_value=1e-6
123 )
124
125 optimizer = optax.chain(
126     optax.clip_by_global_norm(0.5), # Tighter clipping for autoregressive stability
127     optax.adamw(
128         learning_rate=lr_schedule,
129         weight_decay=2e-3, # Increased weight decay for OOD robustness
130         b1=0.9,
131         b2=0.999
132     )
133 )

```

F.4. Solution `sts445`

```

1 import jax
2 import jax.numpy as jnp
3 import flax.linen as nn
4 import optax
5
6 #
7 # CONSTANTS
8 #
9
10 BATCH_SIZE = 512
11 MAX_STEPS = 500_000
12 SCHEDULED_SAMPLING_START_PROB = 1.0
13 SCHEDULED_SAMPLING_FINAL_PROB = 0.0
14 SCHEDULED_SAMPLING_DECAY_STEPS = 400_000
15 EARLY_STOP_PATIENCE = 1500
16 MIN_DELTA = 1e-10
17 LEARNING_RATE = 1e-3
18
19 # NOTE: Connectivity from EPT (cols) to LPT (rows)
20 CONNECTIVITY = [
21     [False, True, True, True, True, True, True],
22     [False, True, True, True, False, True, False],
23     [True, True, True, False, True, True, True, True],
24     [True, True, True, True, True, False, True, False],
25     [True, False, True, True, True, False, False, False],
26     [False, False, True, False, True, False, False, False],
27     [False, True, True, False, False, False, False, True],
28     [False, True, True, True, False, True, True, True],
29     [False, True, True, True, False, False, True, True],
30     [False, False, False, False, True, True, False, False],
31     [False, True, True, True, True, False, True, True],
32     [False, True, True, True, True, True, False, True],
33     [True, True, True, True, False, True, True, True],
34     [True, False, True, False, False, True, True, True],
35     [True, True, True, True, True, True, True, False],
36     [True, False, True, False, True, True, True, True],
37     [True, False, False, False, True, False, True, True],
38     [True, False, False, False, False, False, True, False],
39     [False, False, False, True, False, True, True, False],
40     [False, True, True, True, False, True, True, True],
41     [False, False, True, True, False, True, True, True],
42     [True, True, False, False, False, False, False, False],
43     [True, True, False, False, True, True, True, True],

```

```

44     [True, True, False, True, False, True, True, True]]
45
46     #
47     # MODEL
48     #
49
50     class Candidate(nn.Module):
51         """Hierarchical Neural Dynamic Model with Sparse Connectivity."""
52
53         @nn.compact
54         def __call__(self, past_pred, cov_t, train=False):
55             B = past_pred.shape[0]
56
57             # 1. Decomposition
58             ept_past = past_pred[:, 0:8] # (B, 8)
59             ahb_past = past_pred[:, 32:36] # (B, 4)
60             bout_state = cov_t[:, 0:1] # (B, 1)
61             visual_in = cov_t[:, 1:9] # (B, 8)
62
63             # 2. EPT Update (Neurons 0-7)
64             # Shared dynamics rule across all 8 neurons for OOD robustness.
65             # Inputs: past state, specific visual channel, and global bout state.
66             ept_combined = jnp.stack([ept_past, visual_in, jnp.broadcast_to(bout_state, (B, 8))], axis=-1)
67
68             # Capture second-order interactions [y, v, b, y*v, y*b, v*b]
69             ept_feat = jnp.concatenate([
70                 ept_combined,
71                 ept_combined[..., [0]] * ept_combined[..., [1]],
72                 ept_combined[..., [0]] * ept_combined[..., [2]],
73                 ept_combined[..., [1]] * ept_combined[..., [2]]
74             ], axis=-1) # (B, 8, 6)
75
76             # Shared MLP rule
77             e = nn.Dense(128)(ept_feat)
78             e = nn.leaky_relu(e)
79             e = nn.Dense(128)(e)
80             e = nn.leaky_relu(e)
81
82             # Gated leaky integration for autoregressive stability
83             ept_gate = nn.sigmoid(nn.Dense(1)(e)).squeeze(-1)
84             ept_candidate = nn.sigmoid(nn.Dense(1)(e)).squeeze(-1)
85
86             # Per-neuron individual gain/bias to capture phenotypic variation
87             ept_gain = self.param('ept_gain', nn.initializers.ones, (8,))
88             ept_out = (1.0 - ept_gate) * ept_past + ept_gate * (ept_candidate * ept_gain)
89
90             # 3. LPT Update (Neurons 8-31)
91             # Feed-forward mapping from current EPT, enforcing sparse CONNECTIVITY.
92             mask = jnp.array(CONNECTIVITY) # (24 LPT rows, 8 EPT cols)
93
94             # Two-layer sparse projection
95             lpt_w1 = self.param('lpt_w1', nn.initializers.glorot_uniform(), (24, 8, 32))
96             lpt_b1 = self.param('lpt_b1', nn.initializers.zeros, (24, 32))
97
98             # Each LPT neuron integrates its subset of EPT inputs into a latent space
99             lpt_h = jnp.einsum('bi,nik->bnk', ept_out, lpt_w1 * mask[..., None]) + lpt_b1
100            lpt_h = nn.leaky_relu(lpt_h)
101
102            lpt_w2 = self.param('lpt_w2', nn.initializers.glorot_uniform(), (24, 32, 1))
103            lpt_b2 = self.param('lpt_b2', nn.initializers.zeros, (24,))
104            lpt_out = jnp.einsum('bnk,nko->bn', lpt_h, lpt_w2) + lpt_b2
105            lpt_out = nn.sigmoid(lpt_out)
106
107            # 4. aHB/nMLF Update (Neurons 32-35)
108            # Temporal integrators depending on past state and newly computed LPT.
109            ahb_in = jnp.concatenate([ahb_past, lpt_out], axis=-1) # (B, 4 + 24)
110

```

```
111     a = nn.Dense(256)(ahb_in)
112     a = nn.leaky_relu(a)
113     a = nn.Dense(256)(a)
114     a = nn.leaky_relu(a)
115
116     ahb_gate = nn.sigmoid(nn.Dense(4)(a))
117     ahb_candidate = nn.sigmoid(nn.Dense(4)(a))
118     ahb_out = (1.0 - ahb_gate) * ahb_past + ahb_gate * ahb_candidate
119
120     return jnp.concatenate([ept_out, lpt_out, ahb_out], axis=-1)
121
122 transition_model = Candidate()
123 #
124 # OPTIMIZER
125 #
126
127 lr_schedule = optax.cosine_onecycle_schedule(
128     transition_steps=MAX_STEPS,
129     peak_value=LEARNING_RATE,
130     pct_start=0.1,
131     div_factor=10,
132     final_div_factor=100
133 )
134
135 optimizer = optax.adamw(
136     learning_rate=lr_schedule,
137     weight_decay=1e-5
138 )
139 )
```

G. Supplementary Figures

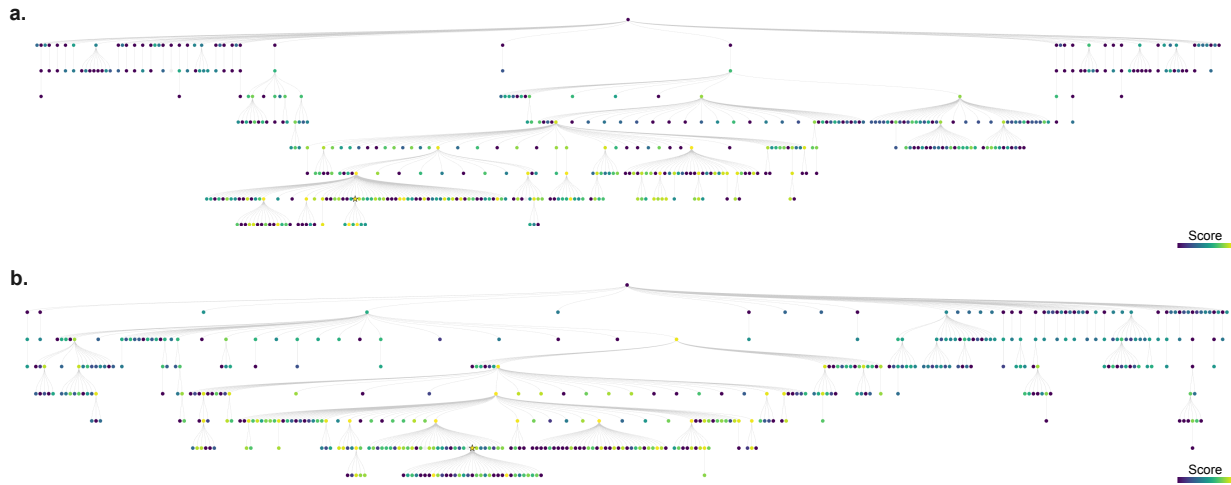


Figure S1 | Full search trees for automated model discovery. Visualization of the complete evolutionary lineage explored by the LLM-guided tree search. Nodes represent executable Python code (candidate models), and edges represent mutations generated by the LLM. Node color indicates the score, with lighter colors representing lower error. **a.** The unconstrained search tree (ts). **b.** The structure-constrained search tree (sts).

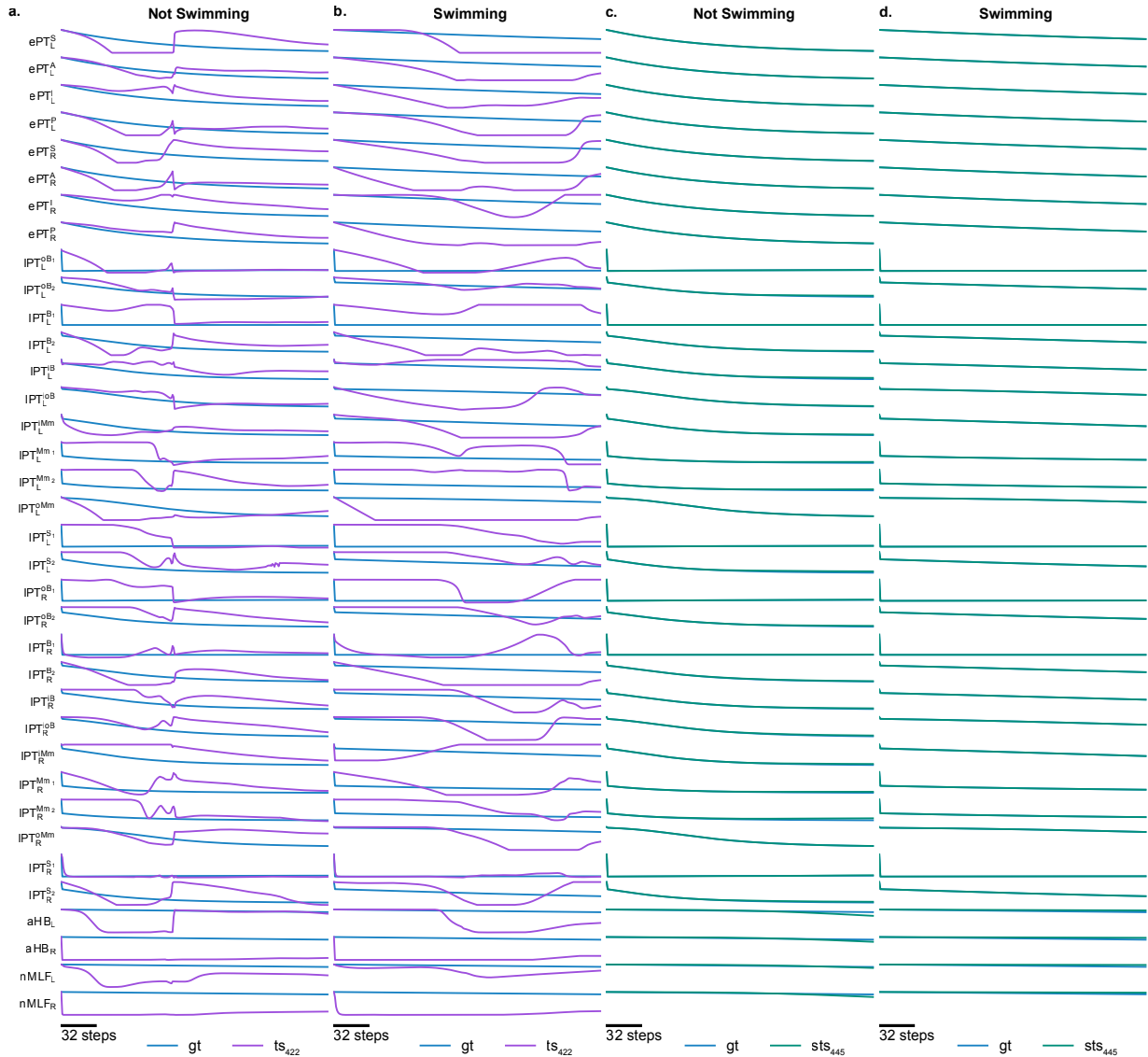


Figure S2 | Impulse response dynamics. We probe the recovery of dynamic mechanisms by the discovered models by initializing all neurons to a saturated state ($a_0 = 1$) and evolving the system for 32 steps under “Not Swimming” (Rest) and “Swimming” conditions. **a, b.** ts_{422} (purple) exhibits erroneous oscillatory behavior, deviating significantly from the ground truth (blue). **c, d.** sts_{445} (green) faithfully reproduces the ground truth state-dependent decay profiles that distinguish swimming from resting dynamics.

H. Supplementary Tables

Table S1 | Performance comparison between best-scoring tree search solutions. In addition to predictive accuracy (MAE), we report mechanistic verification metrics defined in [Appendix C](#): the Frobenius norm of the effective connectivity mismatch (\mathcal{L}_{Jac}) and the impulse response error (\mathcal{L}_{IR}) for both resting and swimming states. The structure-constrained solution (sts_{445}) demonstrates superior mechanistic fidelity compared to the unconstrained one (ts_{422}).

	ts_{422}	sts_{445}
Test MAE ↓	0.00005	0.00001
Holdout MAE ↓	0.13995	0.00027
$\mathcal{L}_{\text{Jac}} \downarrow$	8.33	0.26
$\mathcal{L}_{\text{IR}}^{\text{rest}} \downarrow$	0.27	0.04
$\mathcal{L}_{\text{IR}}^{\text{swim}} \downarrow$	0.29	0.04

Table S2 | Population statistics (median [IQR]) for the top 50 highest-scoring models of each tree search. Aggregated metrics across models discovered during the unconstrained (ts) and structure-constrained (sts) tree searches. The constrained search consistently yields models with lower Jacobian error (\mathcal{L}_{Jac}) and more accurate dynamics (\mathcal{L}_{IR}), indicating that the structural prior effectively regularizes the search space towards higher mechanistic fidelity.

	ts	sts
Test MAE ↓	0.00009 [0.00008, 0.00009]	0.00004 [0.00002, 0.00005]
Holdout MAE ↓	0.00833 [0.00636, 0.02349]	0.00030 [0.00025, 0.00073]
$\mathcal{L}_{\text{Jac}} \downarrow$	7.58 [7.55, 7.73]	0.34 [0.23, 0.45]
$\mathcal{L}_{\text{IR}}^{\text{rest}} \downarrow$	0.14 [0.10, 0.21]	0.03 [0.02, 0.04]
$\mathcal{L}_{\text{IR}}^{\text{swim}} \downarrow$	0.12 [0.09, 0.18]	0.03 [0.02, 0.04]

References

J. Achterberg, D. Akarca, D. Strouse, J. Duncan, and D. E. Astle. Spatially embedded recurrent neural networks reveal widespread links between structural and functional neuroscience findings. *Nature Machine Intelligence*, 2023. URL <https://doi.org/10.1038/s42256-023-00748-9>.

E. Aygün, A. Belyaeva, G. Comanici, M. Coram, H. Cui, J. Garrison, R. J. A. Kast, C. Y. McLean, P. Norgaard, Z. Shamsi, D. Smalling, J. Thompson, S. Venugopalan, B. P. Williams, C. He, S. Martinson, M. Plomecka, L. Wei, Y. Zhou, Q.-Z. Zhu, M. Abraham, E. Brand, A. Bulanova, J. A. Cardille, C. Co, S. Ellsworth, G. Joseph, M. Kane, R. Krueger, J. Kartiwa, D. Liebling, J.-M. Lueckmann, P. Raccuglia, X. Wang, K. Chou, J. Manyika, Y. Matias, J. C. Platt, L. Dorfman, S. Mourad, and M. P. Brenner. An AI system to help scientists write expert-level empirical software. *arXiv preprint*, 2025. URL <https://doi.org/10.48550/arXiv.2509.06503>.

M. Beiran and A. Litwin-Kumar. Prediction of neural activity in connectome-constrained recurrent networks. *Nature Neuroscience*, 2025. URL <https://doi.org/10.1038/s41593-025-02080-4>.

P. S. Castro, N. Tomasev, A. Anand, N. Sharma, R. Mohanta, A. Dev, K. Perlin, S. Jain, K. Levin, N. Elteto, W. Dabney, A. Novikov, G. C. Turner, M. K. Eckstein, N. D. Daw, K. J. Miller, and K. Stachenfeld. Discovering symbolic cognitive models from human and animal behavior. In *International Conference on Machine Learning*, 2025. URL <https://openreview.net/forum?id=dhRXGWJ027>.

S.-A. Chen, C.-L. Li, N. Yoder, S. O. Arik, and T. Pfister. TSMixer: An all-MLP architecture for time series forecasting. *Transactions on Machine Learning Research*, 2023. URL <https://openreview.net/forum?id=wbpxTuXgm0>.

A. Das, W. Kong, A. Leach, S. Mathur, R. Sen, and R. Yu. Long-term forecasting with TiDE. *Transactions on Machine Learning Research*, 2023. URL <https://openreview.net/forum?id=pCbC3aQB5W>.

S. Duan, L. L. Dong, and I. Fiete. From synapses to dynamics: Obtaining function from structure in a connectome constrained model of the head direction circuit. *bioRxiv preprint*, 2025. URL <https://doi.org/10.1101/2025.05.26.655406>.

Google. Gemini 3 Flash: Frontier intelligence built for speed, December 17 2025. URL <https://blog.google/products-and-platforms/products/gemini/gemini-3-flash/>. The Keyword.

Y. Han, T. A. Poggio, and B. Cheung. System identification of neural systems: If we got it right, would we know? In *International Conference on Machine Learning*, 2023. URL <https://openreview.net/forum?id=NkTEhPQCjg>.

Z. Jiang, D. Schmidt, D. Srikanth, D. Xu, I. Kaplan, D. Jacenko, and Y. Wu. Aide: Ai-driven exploration in the space of code. *arXiv preprint*, 2025. URL <https://doi.org/10.48550/arXiv.2502.13138>.

E. Jonas and K. P. Kording. Could a neuroscientist understand a microprocessor? *PLoS computational biology*, 2017. URL <https://doi.org/10.1371/journal.pcbi.1005268>.

R. T. Lange, Y. Imajuku, and E. Cetin. ShinkaEvolve: Towards open-ended and sample-efficient program evolution. *arXiv preprint*, 2025. URL <https://doi.org/10.48550/arXiv.2509.19349>.

J. K. Lappalainen, F. D. Tschopp, S. Prakhyta, M. McGill, A. Nern, K. Shinomiy, S.-y. Takemura, E. Gruntman, J. H. Macke, and S. C. Turaga. Connectome-constrained networks predict neural activity across the fly visual system. *Nature*, 2024. URL <https://doi.org/10.1038/s41586-024-07939-3>.

V. Lobato-Rios, S. T. Ramalingasetty, P. G. Özil, J. Arreguit, A. J. Ijspeert, and P. Ramdya. NeuroMechFly, a neuromechanical model of adult *drosophila melanogaster*. *Nature Methods*, 2022. URL <https://doi.org/10.1038/s41592-022-01466-7>.

I. Loshchilov and F. Hutter. Decoupled weight decay regularization. In *International Conference on Learning Representations*, 2019. URL <https://openreview.net/forum?id=Bkg6RiCqY7>.

L. Mi, R. Xu, S. Prakhya, A. Lin, N. Shavit, A. Samuel, and S. C. Turaga. Connectome-constrained latent variable model of whole-brain neural activity. In *International Conference on Learning Representations*, 2021. URL <https://openreview.net/forum?id=CJzi3dR1JE->.

A. Novikov, N. Vũ, M. Eisenberger, E. Dupont, P.-S. Huang, A. Z. Wagner, S. Shirobokov, B. Kozlovskii, F. J. R. Ruiz, A. Mehrabian, M. P. Kumar, A. See, S. Chaudhuri, G. Holland, A. Davies, S. Nowozin, P. Kohli, and M. Balog. Alphaevolve: A coding agent for scientific and algorithmic discovery. *arXiv preprint*, 2025. URL <https://doi.org/10.48550/arXiv.2506.13131>.

B. Romera-Paredes, M. Barekatain, A. Novikov, M. Balog, M. P. Kumar, E. Dupont, F. J. R. Ruiz, J. S. Ellenberg, P. Wang, O. Fawzi, P. Kohli, and A. Fawzi. Mathematical discoveries from program search with large language models. *Nature*, 2024. URL <https://doi.org/10.1038/s41586-023-06924-6>.

D. Salinas, V. Flunkert, J. Gasthaus, and T. Januschowski. Deepar: Probabilistic forecasting with autoregressive recurrent networks. *International Journal of Forecasting*, 2020. URL <https://doi.org/10.1016/j.ijforecast.2019.07.001>.

G. P. Sarma, C. W. Lee, T. Portegys, V. Ghayoomie, T. Jacobs, B. Alicea, M. Cantarelli, M. Currie, R. C. Gerkin, S. Gingell, P. Gleeson, R. Gordon, R. M. Hasani, G. Idili, S. Khayrulin, D. Lung, A. Palyanov, M. Watts, and S. D. Larson. OpenWorm: Overview and recent advances in integrative biological simulation of *caenorhabditis elegans*. *Philosophical Transactions of the Royal Society B*, 2018. URL <https://doi.org/10.1098/rstb.2017.0382>.

M. Schmidt and H. Lipson. Distilling free-form natural laws from experimental data. *Science*, 324, 2009. URL <https://doi.org/10.1126/science.1165893>.

R. Tilbury, D. Kwon, A. Haydaroglu, J. Ratliff, V. Schmutz, M. Carandini, K. Miller, K. Stachenfeld, and K. D. Harris. Characterizing neuronal population geometry with AI equation discovery. *bioRxiv preprint*, 2025. URL <https://doi.org/10.1101/2025.11.12.688086>.

R. Vaxenburg, I. Siwanowicz, J. Merel, A. A. Robie, C. Morrow, G. Novati, Z. Stefanidi, G.-J. Both, G. M. Card, M. B. Reiser, M. M. Botvinick, K. M. Branson, Y. Tassa, and S. C. Turaga. Whole-body physics simulation of fruit fly locomotion. *Nature*, 2025. URL <https://doi.org/10.1038/s41586-025-09029-4>.

A. Zeng, M. Chen, L. Zhang, and Q. Xu. Are transformers effective for time series forecasting? In *AAAI Conference on Artificial Intelligence*, 2023. URL <https://doi.org/10.1609/aaai.v37i9.26317>.

M. Zhao, N. Wang, X. Jiang, X. Ma, H. Ma, G. He, K. Du, L. Ma, and T. Huang. An integrative data-driven model simulating *c. elegans* brain, body and environment interactions. *Nature Computational Science*, 2024. URL <https://doi.org/10.1038/s43588-024-00738-w>.

B. Zoph and Q. V. Le. Neural architecture search with reinforcement learning. In *International Conference on Learning Representations*, 2017. URL <https://openreview.net/forum?id=r1Ue8Hcxg>.